# INTERIM REPORT

## Sonar Detection and Classification of Underwater UXO and Environmental Parameters

SERDP Project MR-1666

OCTOBER 2010

Raymond Lim
**Naval Surface Warfare Center**

*This document has been cleared for public release*

SERDP
DOD ▪ EPA ▪ DOE

This report was prepared under contract to the Department of Defense Strategic Environmental Research and Development Program (SERDP). The publication of this report does not indicate endorsement by the Department of Defense, nor should the contents be construed as reflecting the official policy or position of the Department of Defense. Reference herein to any specific commercial product, process, or service by trade name, trademark, manufacturer, or otherwise, does not necessarily constitute or imply its endorsement, recommendation, or favoring by the Department of Defense.

# Table of Contents

Sonar Detection and Classification of Underwater UXO and Environmental Parameters ..... 1
Table of Contents ..... ii
Table of Figures ..... ii
Acronyms ..... iii
Sonar Detection and Classification of Underwater UXO and Environmental Parameters ..... 1
Abstract ..... 1
Objective ..... 1
Technical Approach ..... 2
Results ..... 5
Conclusions to date ..... 17
References ..... 18

# Table of Figures

Figure 1. The NSWC PCD freshwater pond facility: 13.7 m deep, 110 m long by 80 m wide with1.5 m thick sand bottom. ..... 3
Figure 2. Targets used in pond scattering measurements. ..... 3
Figure 3. Basic configuration for scattering measurements. ..... 4
Figure 4. Backscatter SAS imagery processed from data collected around target broadside at a 40$^o$ grazing angle. ..... 6
Figure 5. Backscatter acoustic color processed from data collected around target broadside at a 40$^o$ grazing angle. ..... 7
Figure 6. Backscatter spatial frequency vs frequency plot processed from data collected around target broadside at a 40$^o$ grazing angle. ..... 8
Figure 7. Comparison of acoustic color for a 2ft long x 1ft diameter solid Al cylinder processed from data collected in 2008 and 2009. ..... 8
Figure 8. Mesh refinements formulated for scattering by a proud spherical shell. ..... 9
Figure 9. Verification of COMSOL-based FE solution for scattering by a spherical shell. ..... 9
Figure 10. Validation of COMSOL-based FE solution for scattering by a free-field 5:1 solid Al cylinder. ..... 10
Figure 11. FE vs measurement comparison for scattering by a 5:1 solid Al cylinder deployed proud on the sand bottom of the NSWC PCD freshwater pond. ..... 11
Figure 12. PC SWAT is used to imbed targets on the featureless bottom (above left) into the imported image from a previous field survey (above right). ..... 12
Figure 13. Isolation of selected target signals from noisy data. ..... 13
Figure 14. Subtracting the isolated target signal from the original signal. ..... 13
Figure 15. Among a set of 3 like- shaped cylinders, a feature selection tool is applied to look for phenomena in the acoustic color of each target (top row) that is unique to that target (white or black regions in the corresponding plot below). ..... 14
Figure 16. Excitation of surface Rayleigh waves at -27$^o$ target aspect on a solid Al cylinder produces quasi-periodic structure in its acoustic color plot. ..... 15
Figure 17. Process for using elastic information in sonar data to discriminate between 4 cylindrical targets with the same size and shape. ..... 16
Figure 18. Silhouette plot of four clusters in 5 dimensional feature space. ..... 16

# Acronyms

Al - Aluminum
APL-UW – Applied Physics Laboratory at University of Washington
ATR – Automated Target Recognition
CAC – Computer Aided Classification
CAD – Computer Aided Detection
C/ID – Classification/Identification
COMSOL – software trade name, formerly FEMLAB
FE – Finite Element
FEM – Finite Element Method
FY – Fiscal Year
IEEE – Institute of Electrical and Electronics Engineers
kHz – kiloHertz
MATLAB – MATrix LABoratory numerical computing software marketed by Mathworks
NCSC – Naval Coastal Systems Center
NSWC PCD – Naval Surface Warfare Center Panama City Division (formerly CSS and NCSC)
ONR – Office of Naval Research
PC SWAT – Personal Computer Shallow Water Acoustic Toolset
SAS – Synthetic Aperture Sonar
SNR – Signal-to-Noise Ratio
SON – Statement of Need
T-matrix – Transition matrix
UXO – UneXploded Ordnance
WSU – Washington State University
X – NSWCPCD organizational code

# Sonar Detection and Classification of Underwater UXO and Environmental Parameters

POC: Dr. Raymond Lim
Naval Surface Warfare Center Panama City Division, Code HS-11, 110 Vernon Ave.
Panama City, FL, 32407, 850-235-5178, raymond.lim@navy.mil

## Abstract

Based on extensive assessments of other sensor technologies carried out at NSWCPCD for underwater Navy applications, sonar is expected to play an indispensible role in underwater UXO remediation. Acoustics can be used to probe for targets over a significant range and, being a wave phenomenon, can be used to image buried targets for discrimination from clutter. However, environmental factors can make detection and discrimination problematic. The objective of the current research is to work towards resolving issues that affect sonar detection and classification/identification (C/ID) of underwater UXO using sonar. This is accomplished by leveraging on-going Navy sponsored sonar tests to collect data to both further the model validation needed to keep sonar models and simulations such as PC SWAT up to date for UXO applications and to develop and evaluate C/ID algorithms for separating UXO from bottom clutter. As part of the model validation process, we continue to develop ways to measure environmental parameters required as model inputs. As part of the C/ID process we propose to identify clues in sonar signals that could be used to classify detected UXO and to assess the robustness of these clues to environmental factors. Without a classification capability, true sonar performance against desired targets is difficult to measure. These proposed efforts are meant to respond to SERDP SON MMSON-09-01.

## Objective

MMSON-09-01 specifies needs for studies focusing on "wide area assessment" and the "acoustic response of munitions and environment" in underwater areas. The research performed in this project responds to these points by investigating issues associated with using sonar as a tool for finding and characterizing UXO. Sonar has been the Navy's workhorse for detection and discrimination of underwater objects from clutter through analysis of image features. However, new features need to be identified for UXO due to their more varied shapes and sizes, and difficulties arise for buried ordnance (like most UXO) because the wave attenuation and inhomogeniety in ocean sediments make detection less predictable and high-resolution imaging more difficult. Even when imaging can be done, important image features (e.g., highlight/shadow features) are lost. Therefore, modeling, data collection, and data analysis is performed as a primary component of this project to develop the understanding of factors that affect the acoustic response of proud and buried munitions when searched with both side-scan sonar used for wide area assessment and bottom-looking sonar for detection of completely buried targets. The knowledge gained would be used to

- test new ways to improve signal-to-noise (SNR) against targets
- improve ability to discriminate UXO from clutter

- validate simulation software for generating sonar data
- enable UXO sonar performance prediction.

A particular interest in this effort is on identifying target phenomena yielding features with robust discriminatory power for separating UXO from clutter. This interim report will summarize the results obtained towards these goals based on the modeling, data collection, and data analysis performed during the first half of this project.

## Technical Approach

The approach taken to enable wide area assessment of UXO contamination with sonar is to build a high fidelity simulation capability that can be used to test overall performance of various sonar under varying conditions. At NSWC PCD, simulation of image-based sonar performance has generally been carried out using software such as the Personal Computer Shallow Water Acoustic Toolset (PC SWAT), so improving and validating this software for UXO applications with insight gained from modeling and data analysis continues to be done as needed. However, growing concerns over small or buried targets that are difficult to image to the resolution needed for effective classification has driven a need to extract either more or different information from the target response. To meet this need, this project investigates and compares the detection and discriminatory potential of target information collected and/or processed and combined in different ways.

The best information to extract from the target response has yet to be determined. However, recent efforts fusing target aspect and spectral characteristics from backscatter echoes has been shown to yield potentially good features for distinguishing targets from clutter. This was demonstrated by training statistical pattern recognition algorithms such as support vector machines and relevant vector machines with feature vectors extracted from the target aspect vs frequency data. Thus, high resolution imagery is not required. While use of these statistical tools for automated target recognition (ATR) is growing, a danger is that insufficient training can produce good classification using existing data sets with little assurance of robustness against new data sets. Robust discrimination depends on training with data sets that sufficiently sample the range of feature variability that targets and clutter can exhibit, which is typically not known *a priori* and can require a large amount of training data. Because collecting sufficient data for training can be very costly, the approach taken to help test the ATR component of sonar performance combines results of several efforts to make sure a diverse set of data for classifier training and testing is created. First, dedicated UXO and clutter measurements in NSWC PCD's pond facilities (Fig. 1) are carried out to provide a controlled dataset of realistic target responses. This is further supplemented with leveraging the Navy's investment in the development of an efficient, high-fidelity, Finite Element (FE) simulation capability that can accommodate complex targets in realistic environments. Physics-based interpretations of target responses are used to select target characteristics to draw features from for ATR use. The premise is that training data requirements can be reduced if target characteristics known to be unique to UXO can be found. More details for these efforts are as follows.

**Controlled pond measurements:** Drs. J. Kennedy and J. Lopes performed pond measurements in NSWC PCD's pond facility (Fig. 1) in collaboration with researchers from the University of

**Figure 1. The NSWC PCD freshwater pond facility: 13.7 m deep, 110 m long by 80 m wide with1.5 m thick sand bottom.**

Washington Applied Physics Laboratory (APL-UW) (Drs. S. Kargl and K. Williams) and researchers from Washington State University (WSU) (Prof. P. Marston). Bottom target scattering measurements were carried out on a set of realistic and canonical shaped targets (Fig. 2) chosen to allow both variety for ATR analysis and simplicity for benchmarking and facilitating physical interpretation. Measurement configurations were set up to collect data in monostatic (co-located source and receiver) and bistatic (not co-located) modes against targets

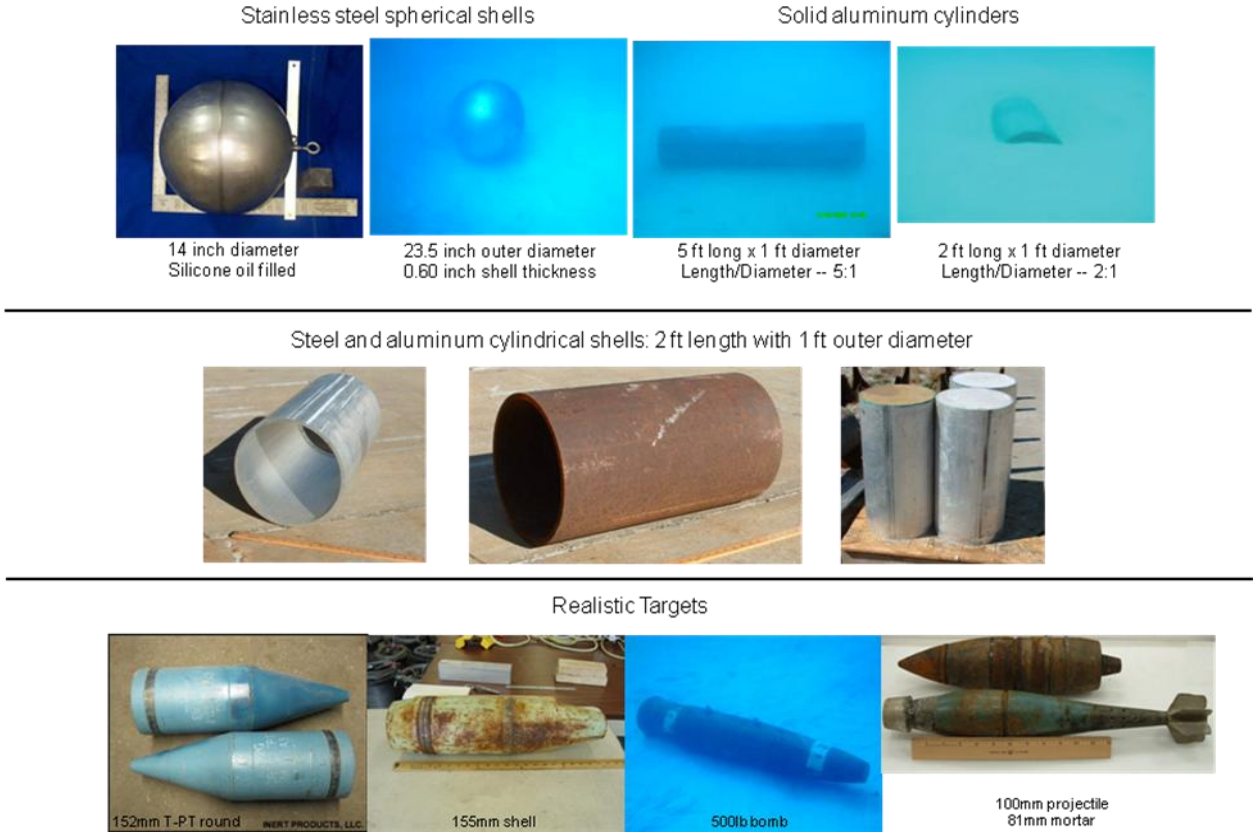


**Figure 2. Targets used in pond scattering measurements.**

that were both proud and buried and illuminated at above and below the critical grazing angle of the bottom. Targets were typically oriented with their axes parallel to the bottom surface but some data on a cylinder tilted up at the surface was also collected. Data was collected using two rails deployed on the sand bottom in a basic arrangement as depicted in Fig. 3. Sources and receivers attached to towers moved along the rails allowed synthetic aperture sonar (SAS) data to be collected over a frequency band of 3-50kHz.

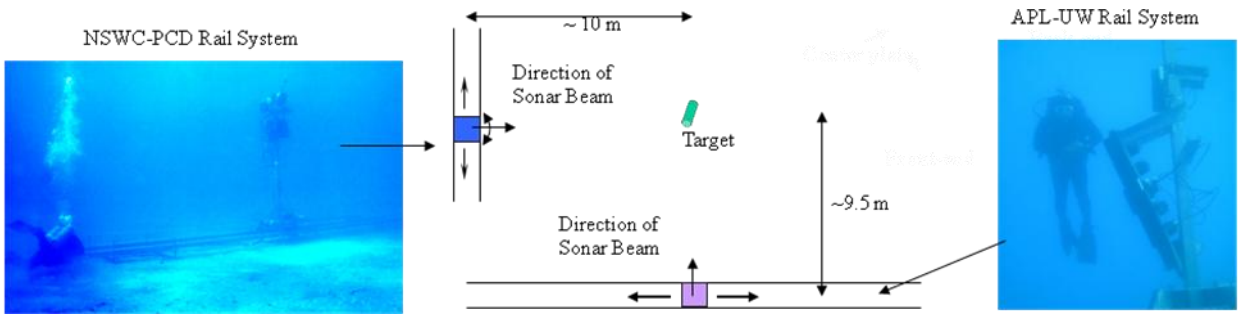


**Figure 3. Basic configuration for scattering measurements.**

**Finite Element (FE) simulation:** Development of a capability to carry out finite element simulations for realistic targets on or in the seafloor has been funded for several years at NSWC PCD by the Office of Naval Research (ONR). The present project leverages this work to help extend its use for building a database of UXO target signatures. The approach taken so far has been to develop and check a set of algorithms written for the COMSOL Multiphysics software package. These produce highly efficiently gridded solutions for elastic targets on or buried under a typical ocean bottom. Solution grid configurations and sizes were formulated to maintain uniform error across specified frequency bands. Reduced grid size formulations taking advantage of target symmetries were introduced. Boundary conditions that allowed reduced FE volume sizes around elongated targets were derived and tested. Coupling the FE solutions to analytic propagation formulas based on the Helmholtz equation was performed to allow fast simulations out to long ranges. Verification and validation of much of these FE components on a set of proud and buried canonical targets (spheres and cylinders) was performed by comparing against benchmarks computed with transition matrix solutions. Tests of the existing FE system have mostly been run on dedicated workstations but the current FE software has recently been transported to a scalable architecture, 25 processor, multi-blade rack computer. Thus, computational turnover can potentially be increased by a factor of 25 by distributing portions of long runs among the processors. With incorporation of the latest COMSOL upgrade, parallel processing of complex problems will also be possible.

**Processing and ATR training tools:** While the measurements and FE simulations performed will provide data that can be used to train and test ATR algorithms for non-image based classification, software tools were also developed to increase the effectiveness of this data. A capability has been developed using PC SWAT to imbed target data either collected or simulated into imagery from past field surveys; thus, making available an infinite number of new target-in-environment combinations that can be processed for imagery or other target spaces to be fed into

ATR classifiers. This is further enabled by developing and applying algorithms for isolating target signals from given measured data sets so they can be swapped into other data sets. The resulting target signal isolation algorithms also make data collection more efficient by allowing simultaneous sonar measurements on multiple targets within a limited area. Even though their signals overlap in the SAS data, signals for each target can be separated and subsequently processed into imagery or aspect vs frequency space for feature extraction. Finally, an algorithm has been produced to help select the best features for class separation among similarly shaped targets.

## Results

Results from the first half of project MM-1666 are described below according to the major tasks performed: controlled measurements and data analysis, FE development and modeling, and classification analysis.

**Controlled measurements and data analysis:** Two major test events were carried out during 2009 and 2010 in collaboration with APL/UW and WSU in NSWC PCD's freshwater test pond. These involved targets deployed on a flat sand bottom at various depths. SAS data were acquired using both monostatic and bistatic scattering configurations to investigate the potential advantages of nonstandard sonar detection and classification configurations. Some initial results and analysis of data from the pond tests were published in papers [2] and [3], which are attached in the Appendix for further detail. To assess the relative advantages of different representations of the target, the data were processed in three ways: imagery, projections onto target aspect angle vs frequency ("acoustic color") space, and projections onto spatial frequency vs frequency space. The last is produced as an intermediate step in wavenumber algorithm beamforming [1] and is, therefore, of interest for extracting additional target information that efficiently complements imagery. Examples of these representations are shown in Figs. 4-6 for backscatter by 4 proud targets (2ft Al cylinder, 2ft pipe, bullet shape, and mortar) insonified at a $40^{o}$ grazing angle.

In general, all three representations of the 4 targets produce useful distinguishing characteristics. For example, in Fig. 4, the cylindrical shapes are easily distinguished from the bullet and mortar by their shape and dimensions. Even the two cylinders exhibit distinctly different reverberation and elastic reradiation patterns. However, despite adequate SNR for detection, the smaller bullet and mortar shapes are more difficult to distinguish between because the resolution is insufficient to produce unambiguous shapes and dimensions. For these targets, representations like those in Figs. 5 and 6 may be more useful because they focus on properties of the isolated target signal rather than using image characteristics that depend on differences between signals from various parts of the target and the background. Thus, the characteristics observed in Figs. 5 and 6 do not require high spatial resolution but they can be sensitive to the environment.

From the standpoint of classification, it is desirable to project target signals onto spaces that exhibit phenomena unique to the target and that remain robust to changes in the environment. A preliminary look at the issue of environmental sensitivity was addressed with SAS backscatter data collected in 2008 and 2009 and projected onto a target acoustic color space. Measurements on a proud 2ft long x 1ft diameter solid Al cylinder carried out in 2008 were repeated during the

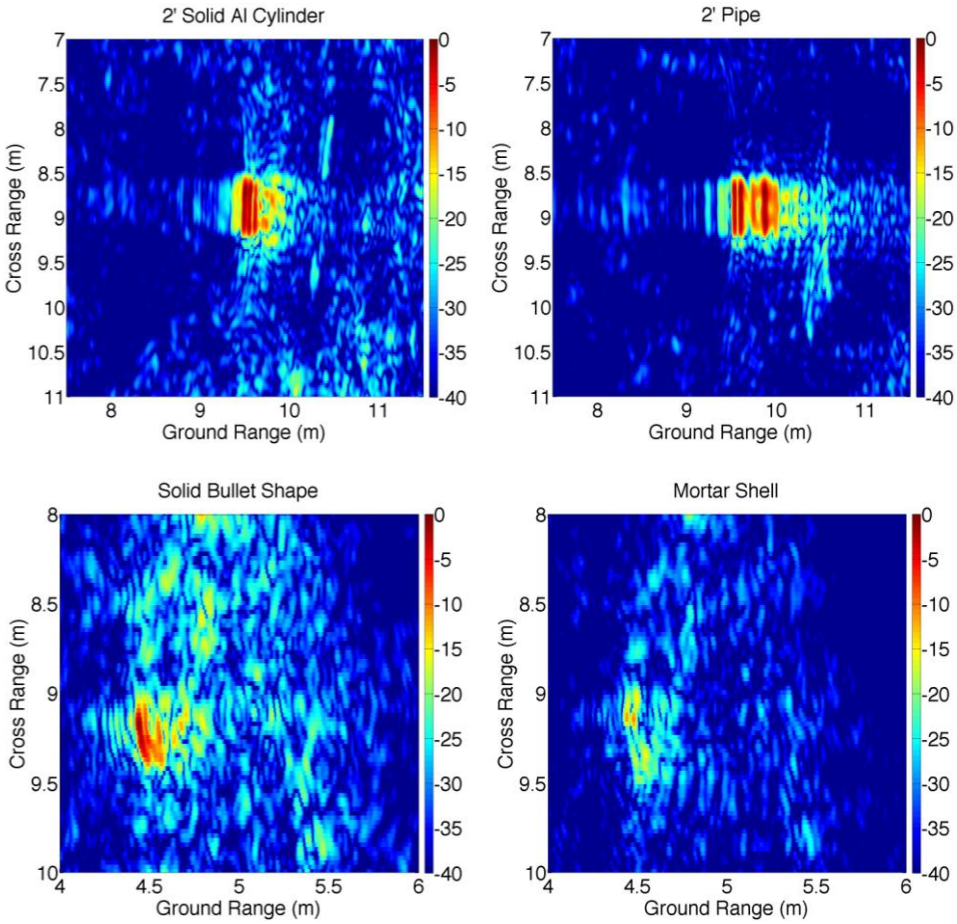


**Figure 4. Backscatter SAS imagery processed from data collected around target broadside at a 40$^o$ grazing angle.**

2009 test to test repeatability of the measurements. A comparison of the resulting acoustic color plots is shown in Fig. 7. Clear differences arise in the two cases. Of particular note is the generally weaker end-on response (90$^o$) in 2009 and the apparent loss in 2008 of the elastic cylinder resonance at 6.6kHz and 50$^o$ aspect. Preliminary calculations suggest these differences are, at least partially, due to a modification of the interference between the specular echo from the target and the echo that includes a single bounce off the bottom. More simply, in FY 2008, the sand surface behaved more like a soft boundary and, in FY 2009, it behaved more like a hard one due to consolidation, resulting in a phase shift in the reverberant echo component. Additional data collected after the sediment was stirred up by divers using a dredge system (used for target burial) and allowed to resettle, produced an acoustic color plot similar to that obtained in FY 2008.

It is notable that subtle differences in the properties of a sand bottom can lead to fairly significant differences in the acoustic color plot of a target. This comparison emphasizes the care needed when preparing data sets for training of statistics-based classification algorithms. A set that exhibits the full range of variation induced by the environments that a target can appear in should

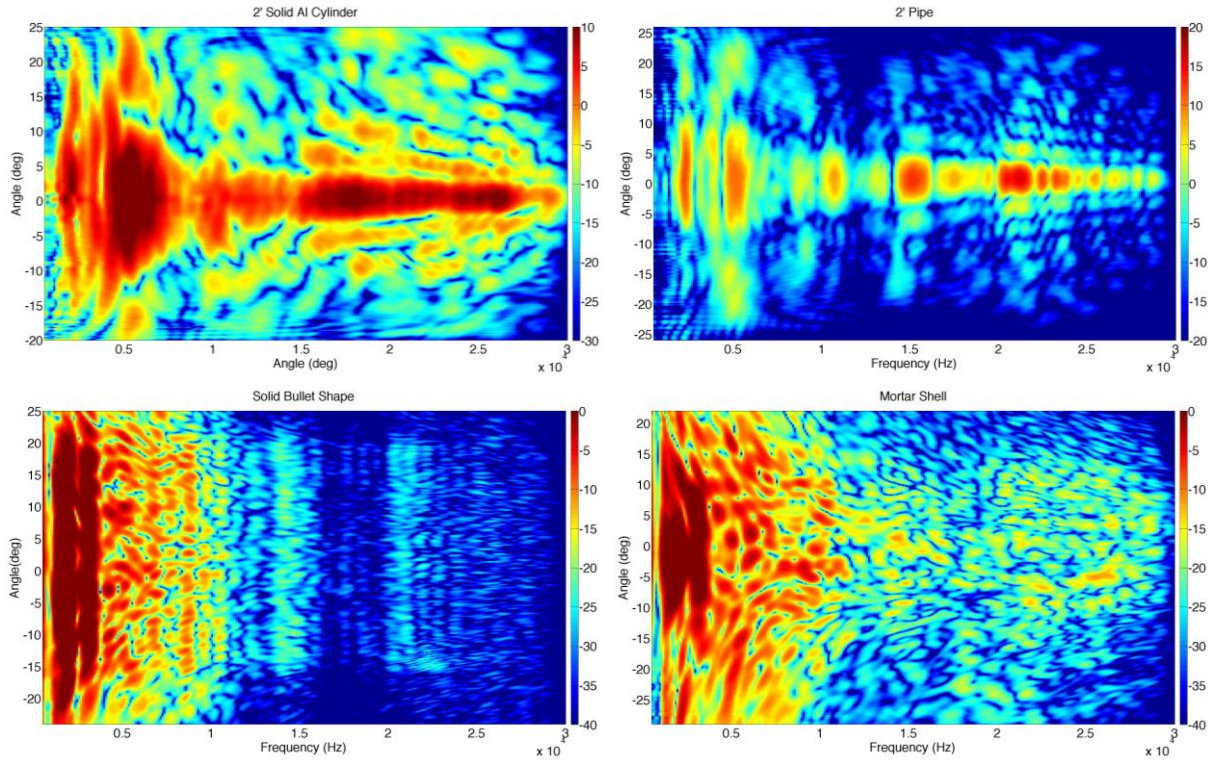


**Figure 5. Backscatter acoustic color processed from data collected around target broadside at a 40$^o$ grazing angle.**

be used. Otherwise, in the present case, algorithms trained on 2008 data might not recognize the same target in 2009.

**FE development and modeling:** The development of a FE capability for UXO sonar simulations is proceeding towards maturity with several checks of the fidelity of calculations having been performed for canonical target shapes on a sand bottom (D. Burnett, R. Lim, NSWC PCD). Due to the envisioned complexity of real targets, a considerable effort was made to formulate efficient meshes for shelled structures interacting with an ocean interface like the seafloor. Mesh refinements were formulated to automatically maintain only the calculation load needed to maintain a nominally uniform error across a wide frequency band. Some of these refinements are illustrated in Fig. 8 for one of the benchmark comparisons using a spherical shell.

Verification of these refinements for scattering by a 5%-thick, stainless-steel, spherical shell insonified at high (40$^o$) and low (20$^o$) grazing angles under proud, half-buried, and buried configurations is demonstrated in Fig. 9. Although verification studies must be carried out using simple targets because high-accuracy benchmark solutions of the underlying linear acoustic equation are required, the refinements imposed on the FE solution of these targets are expected to be effective for all targets.

Validation of the underlying linear acoustic equations solved with the FE solution engine in COMSOL was also checked by comparing the computed target strength acoustic color of a solid Al cylinder of 5:1 aspect ratio with carefully controlled free-field measurements provided by

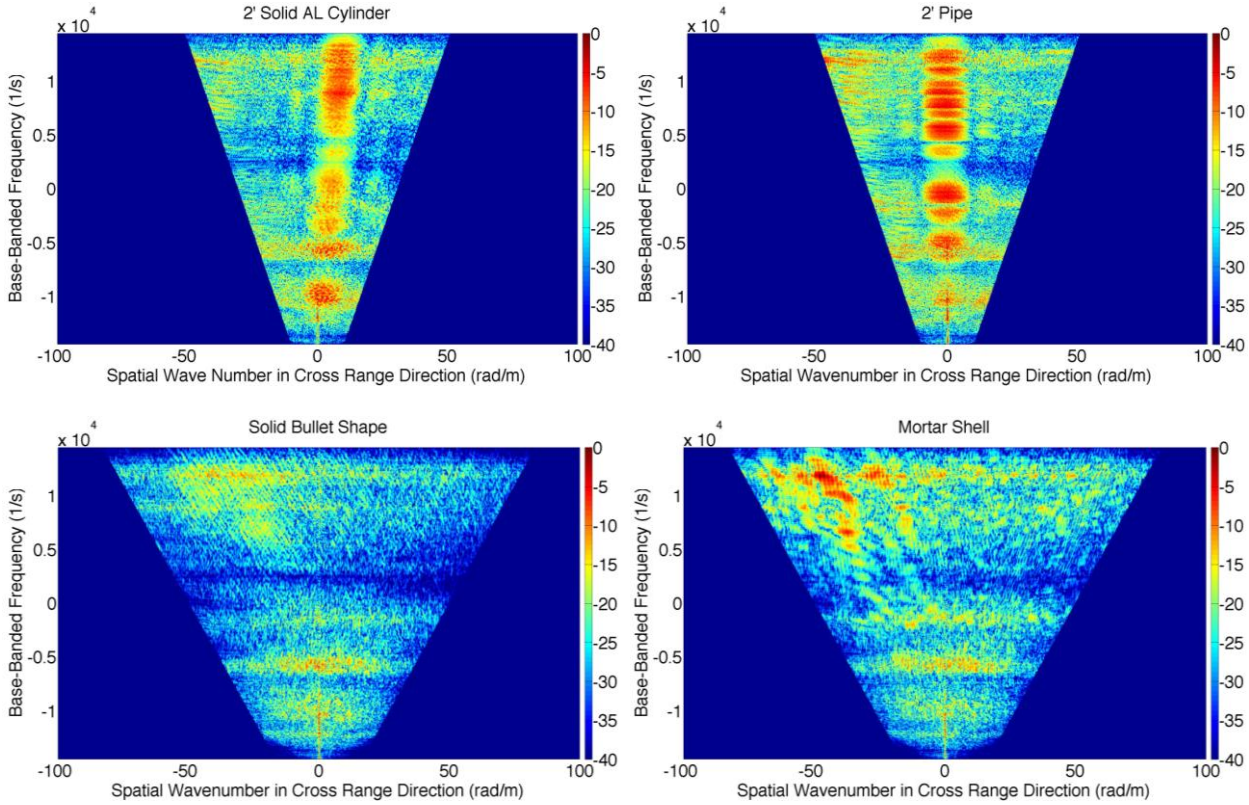


**Figure 6. Backscatter spatial frequency vs frequency plot processed from data collected around target broadside at a 40$^{o}$ grazing angle.**

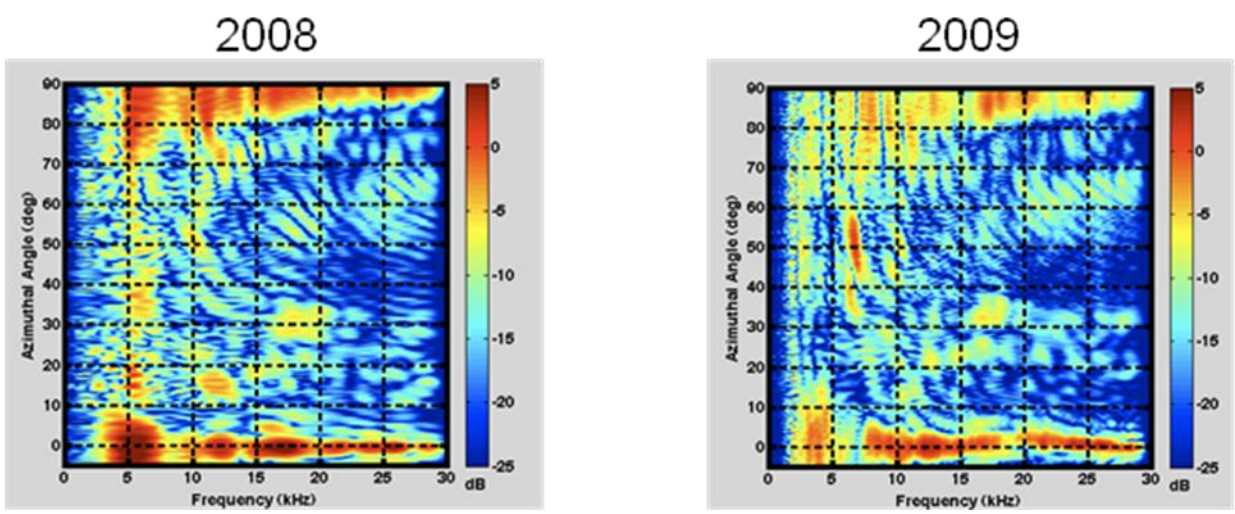


**Figure 7. Comparison of acoustic color for a 2ft long x 1ft diameter solid Al cylinder processed from data collected in 2008 and 2009.**

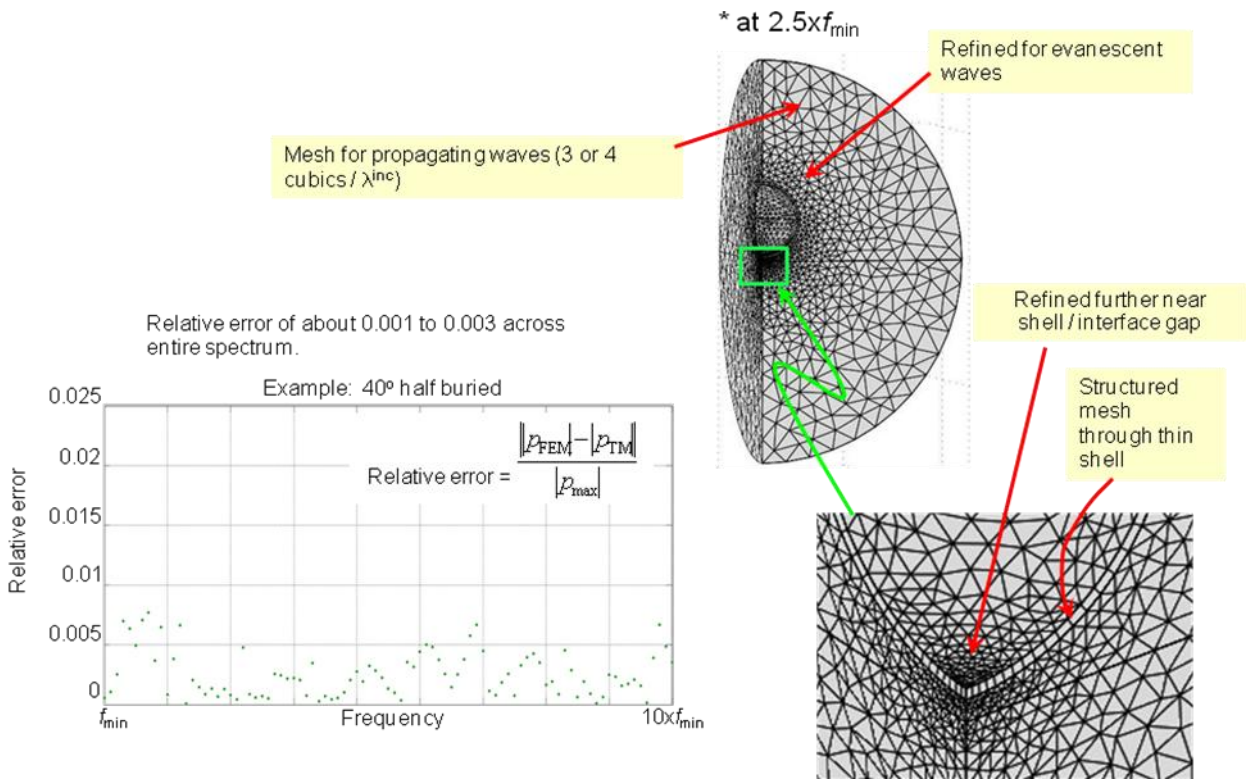


**Figure 8. Mesh refinements formulated for scattering by a proud spherical shell.**

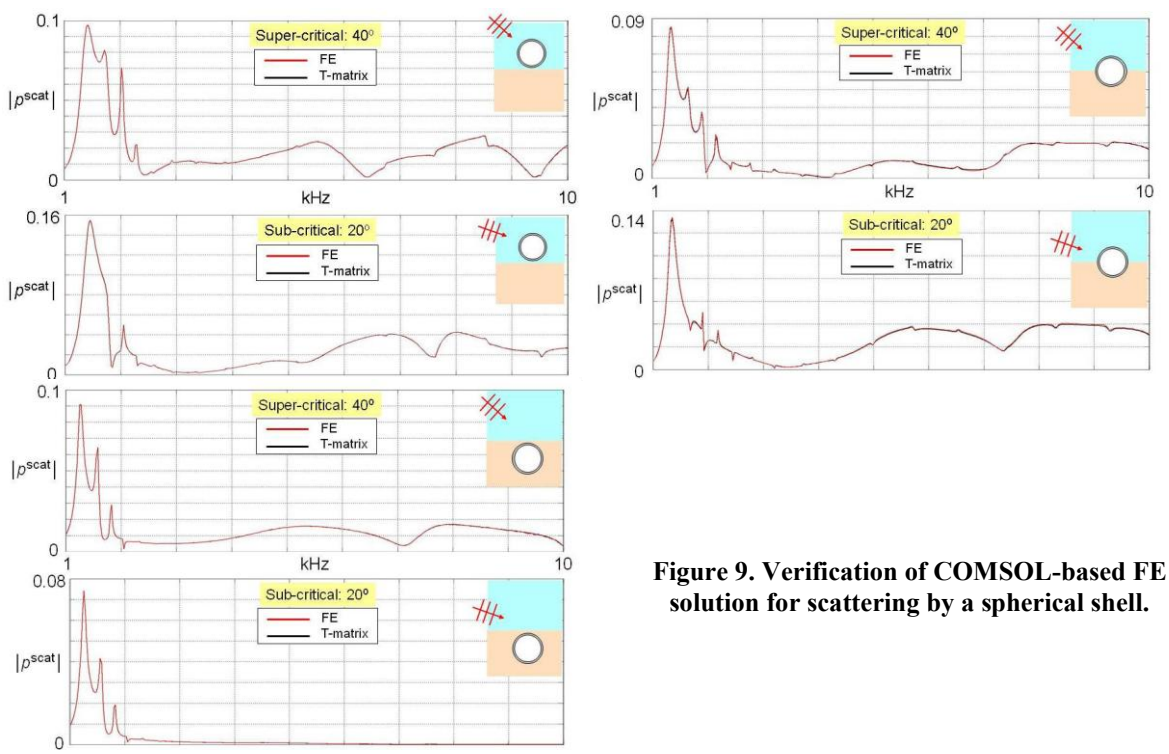


**Figure 9. Verification of COMSOL-based FE solution for scattering by a spherical shell.**

WSU (P. Marston and K. Baik). This is shown in Fig. 10. Agreement is seen to be very good with some small discrepancies that can be attributed to limits on what can be controlled in the measurements: e.g., not having the exact material parameters for the Al cylinder as FE inputs, small variations in uniformity of the material properties of the target, limited experimental SNR, or lower measurement resolution than produced in the FE computation. Lower measurement resolution can be the result of limited tank size, which limits the amount of raw time-domain signal that can be collected before contaminating wall reverberation appears. Nonetheless, the range of agreement seen here is likely the best that can be expected when comparing with measurements.

As the FE capability continues to mature, it is being applied to help interpret observations of scattering by bottom targets. In Ref. [1], FE simulations were used to elucidate environmental effects observed on scattering by a proud Al cylinder on a sand bottom. Figure 11 compares the FE computed target strength in acoustic color space with measured values from 2009 in the NSWC PCD pond (right-hand side of Fig. 7) using the measured sand parameters appropriate for an assumed fluid bottom. Here, the differences were initially thought to be due to neglecting the shear elasticity of the bottom in the FE calculation since the sand was reported to be compacted and hard by divers. Since no shear speed measurements of the sand bottom were possible during the test, the measurement could not be modeled with this bottom property included. However, FE calculations allowing shear speeds in the bottom did not produce the phase shift needed in the surface reflection coefficient to reproduce the observed differences unless the shear speed was chosen outside a realistic range. Resolution of these differences remain under investigation.

In ongoing work, FE simulations are proceeding to more complex targets and target orientations with a systematic focus on developing efficient solutions with controlled accuracy. Simulations on a free-field air-backed cylinder have been completed. Further simulations of target strength acoustic color with this target in various configurations on a sand bottom are under way. These

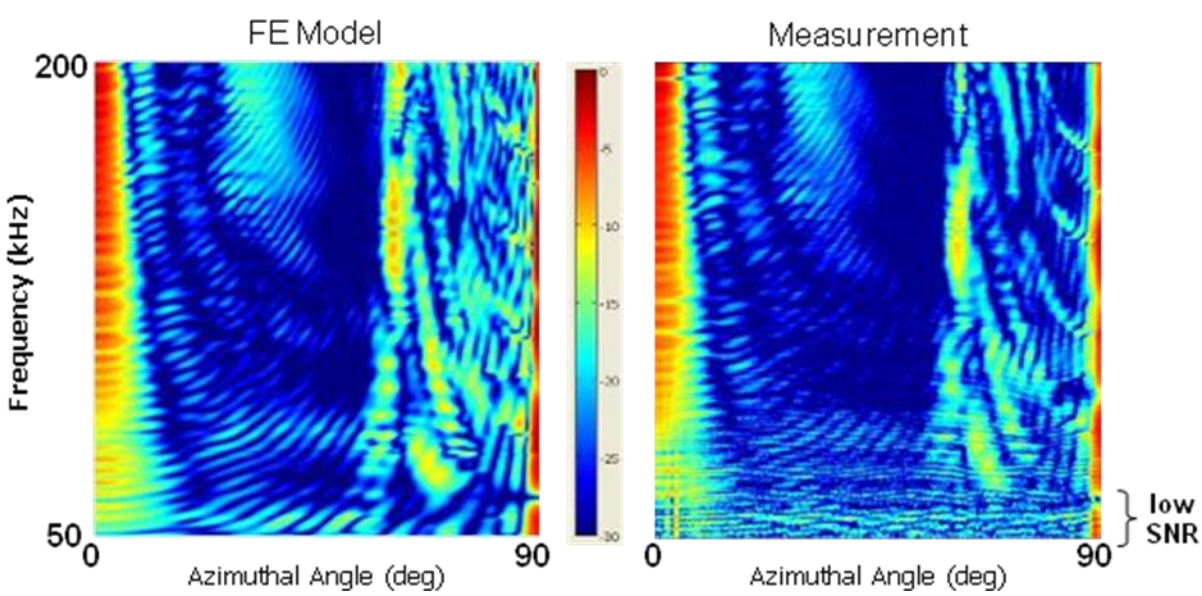


**Figure 10. Validation of COMSOL-based FE solution for scattering by a free-field 5:1 solid Al cylinder.**

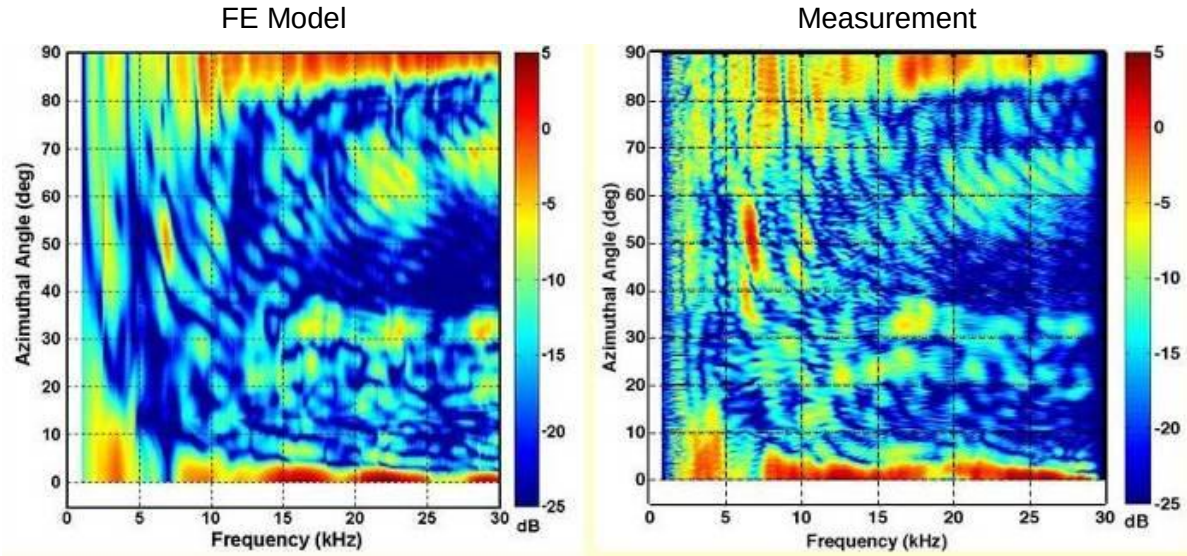


**Figure 11. FE vs measurement comparison for scattering by a 5:1 solid Al cylinder deployed proud on the sand bottom of the NSWC PCD freshwater pond.**

will be used in tests of classification algorithms under development. Other simulations planned are the Al cylinder oriented with a vertical tilt at the sediment surface and the solid bullet shape. Software updates to transport simulations to the new 25 processor rack computer have been performed and initial test runs are proceeding to uncover problems.

**Classification analysis:** In addition to capturing data on targets to train and test classifiers, ways to ensure enough data is captured to produce robust classification were developed. One of these methods imbeds new targets into imagery from past surveys in different environments (G. Sammelmann, NSWC PCD). This is done by importing actual images from a given sonar system into PC SWAT, where the image is normalized and a reflectivity map is created as a function of the x and y coordinates of a point on the bottom. This reflectivity map is used to normalize the direct path bottom reverberation computed by PC SWAT. This procedure allows PC SWAT to compute the raw stave data needed to reproduce the original image in addition to other noise sources and targets.

Because phase information is not known from the original image, this process does not ensure the targets are imbedded into the same bathymetry in the originally surveyed area but it is a more realistic way to combine environmental effects with target signals than adding randomly generated band-limited noise. The user can imbed an arbitrary target into an existing image with minimal artifacts and reverberant reflections from the target and bottom are consistently phased in the raw data. Absolute scattering levels from the original survey are also not known so the relative level is chosen to produce a realistic overall SNR. Target signals collected in other tests or simulated with tools such as FE can also be appropriately scaled and summed into data reconstructed from the reflectivity maps to create new data sets. This method is illustrated in Fig. 12.

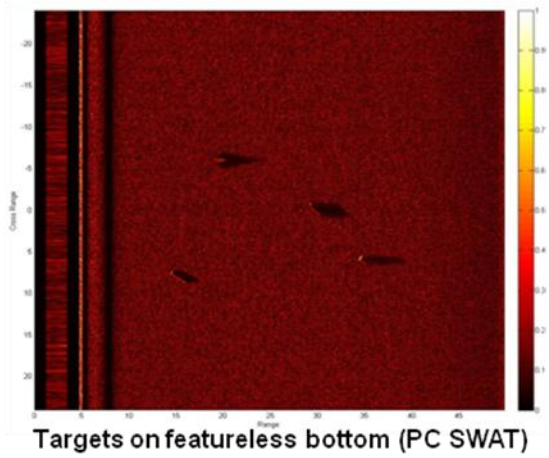


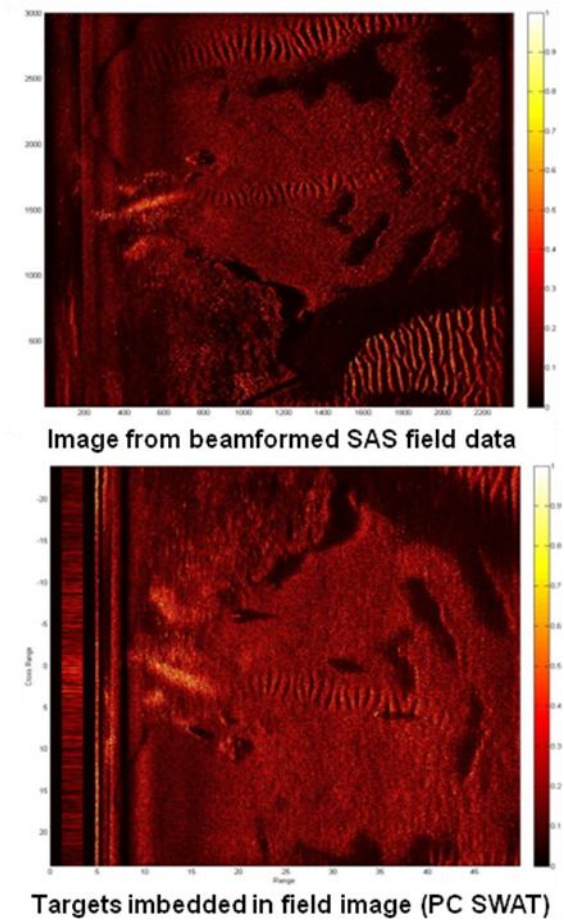


**Figure 12. PC SWAT is used to imbed targets on the featureless bottom (above left) into the imported image from a previous field survey (above right).**

Another way to capture more data for ATR use is to make data collection more efficient. Toward this end, an algorithm was written in MATLAB (T. Marston, NSWC PCD) to allow efficient isolation of target signals for subsequent processing into other target representations; e.g., acoustic color. Figure 13 illustrates the technique. The algorithm beamforms raw SAS data to image a limited range interval where multiple targets appear, so that signals associated with a target of interest can be isolated by cropping out the others in image space. The isolated image is then inverse transformed back to the original data space to obtain a set of raw target signals without contamination from other nearby targets or clutter. The resulting signals can then be reprocessed into a full image of the target area with the isolated target only or into another non-image space. The basic algorithm includes a user-friendly routine to simplify the signal isolation by allowing the user to select the region relevant to a given target using a mouse-drawn box. The effectiveness of the signal isolation was checked by demonstrating that subtracting the isolated target signals from the original data eliminates only the selected target from the original image, as illustrated in Fig. 14. Provided targets are separated by a great enough distance to be resolved by beamforming and care is used in cropping the target in image space, very good isolation is expected. This technique was used extensively to process acoustic color plots from the 2010 pond measurement. Typically, to maximize measurement efficiency, 5-6 targets were deployed simultaneously with only 1-2m separation in the target area, resulting in significant overlap of target signals in the raw data so that standard processing of acoustic color for individual targets would be unavoidably contaminated.

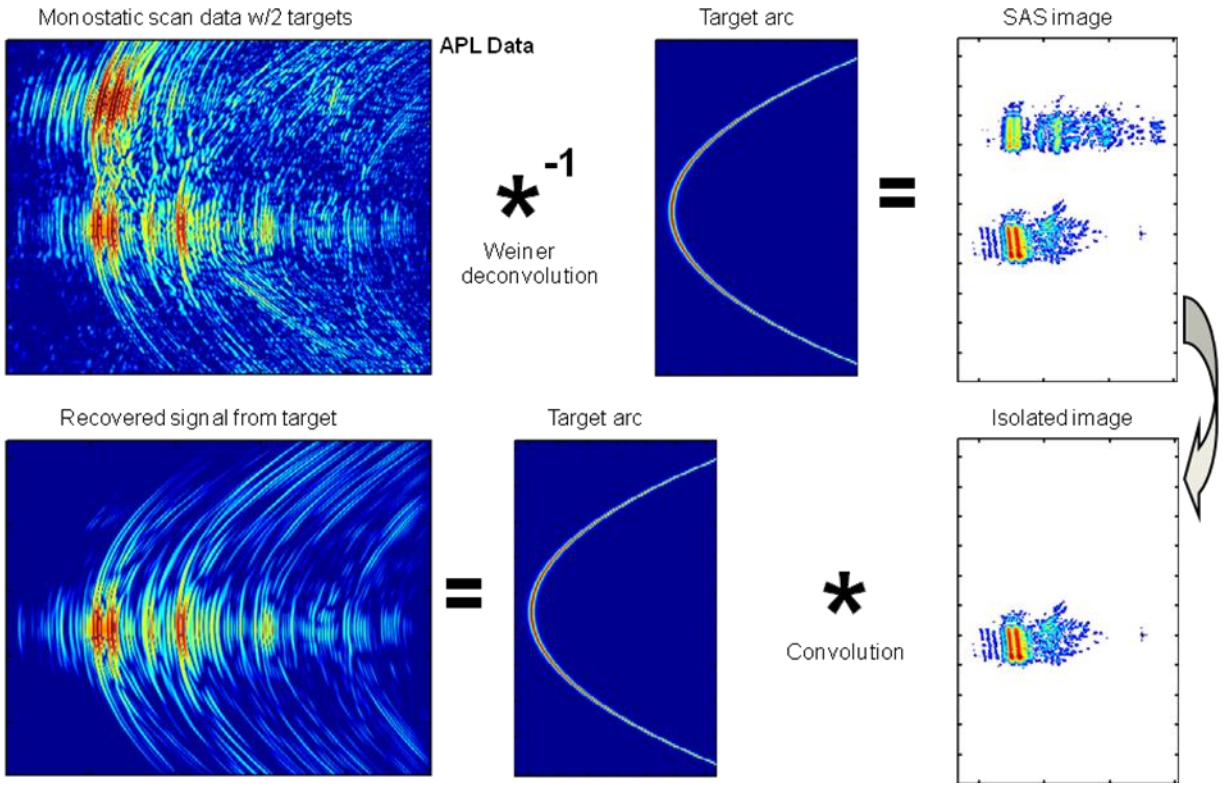


**Figure 13. Isolation of selected target signals from noisy data.**

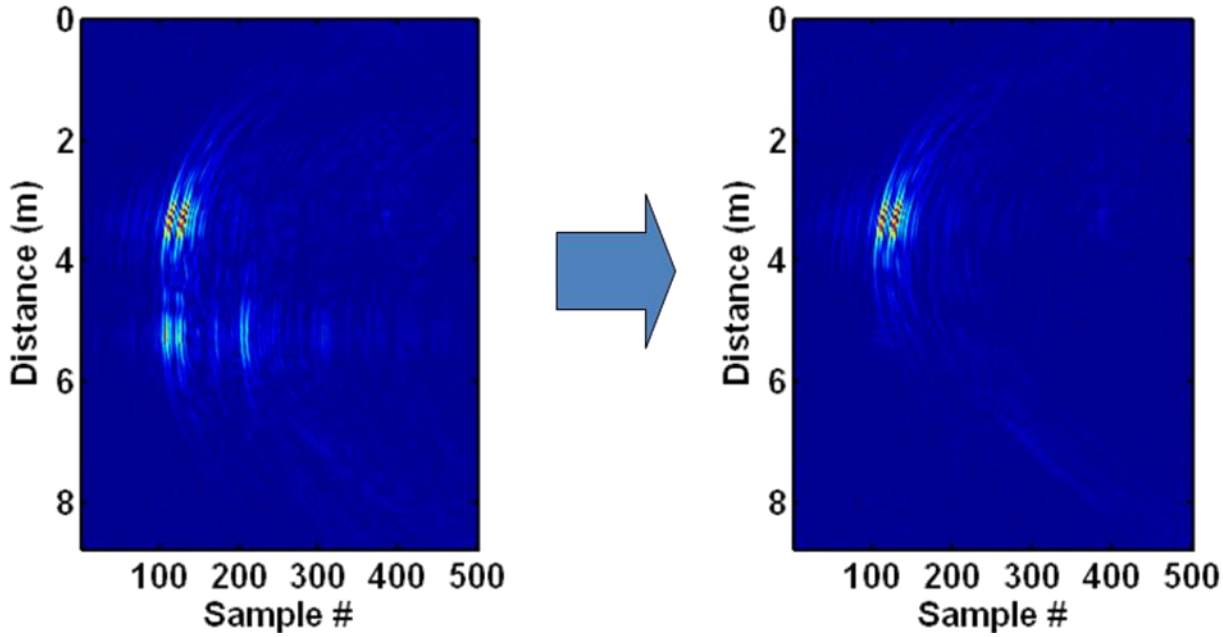


**Figure 14. Subtracting the isolated target signal from the original signal.**

A tool was also developed to help select optimal features for class separation among similarly shaped targets (G. Dobeck, NSWC PCD). The rationale for looking at these types of targets is to help isolate specular phenomena from elastic ones so that the value of classification features derived from the last can be studied. This would be relevant for distinguishing UXO of the same type that are live versus inert. Figure 15 illustrates the variation possible. The top row shows measured free-field target strength plots as a function of frequency and aspect angle for three 2ft-long by 1ft-diameter cylinders of differing material contruction. In the bottom row, potential features are shown for each cylinder in the frequency/aspect space. White areas correspond to regions where the corresponding target exhibits target strength at least 3dB higher than the other two. Black areas correspond to regions where the corresponding target exhibits target strength at least 3dB lower than the other two. Gray areas indicate common target strength levels. At least for this limited data set, it is clear that extracting features from the non-gray areas should result in effective separation of any of the 3 targets shown from the remaining two with no error. Of course, a more practical discriminator would be able to distinguish these targets from a feature set measured under a variety of conditions. While 3dB was chosen here as the threshold for highlighting discriminatory phenomena in the target's acoustic color space, it is anticipated that increasing this threshold can help find phenomena to extract more optimal features for use in a classifier being trained with target data collected under a variety of conditions.

In addition to the tools above for augmenting a statistically-based classification process, a physics-based technique was investigated for distinguishing between a similar set of 4 cylindrical targets (R. Arietta, NSWC PCD). Physics motivated classification can help mitigate training

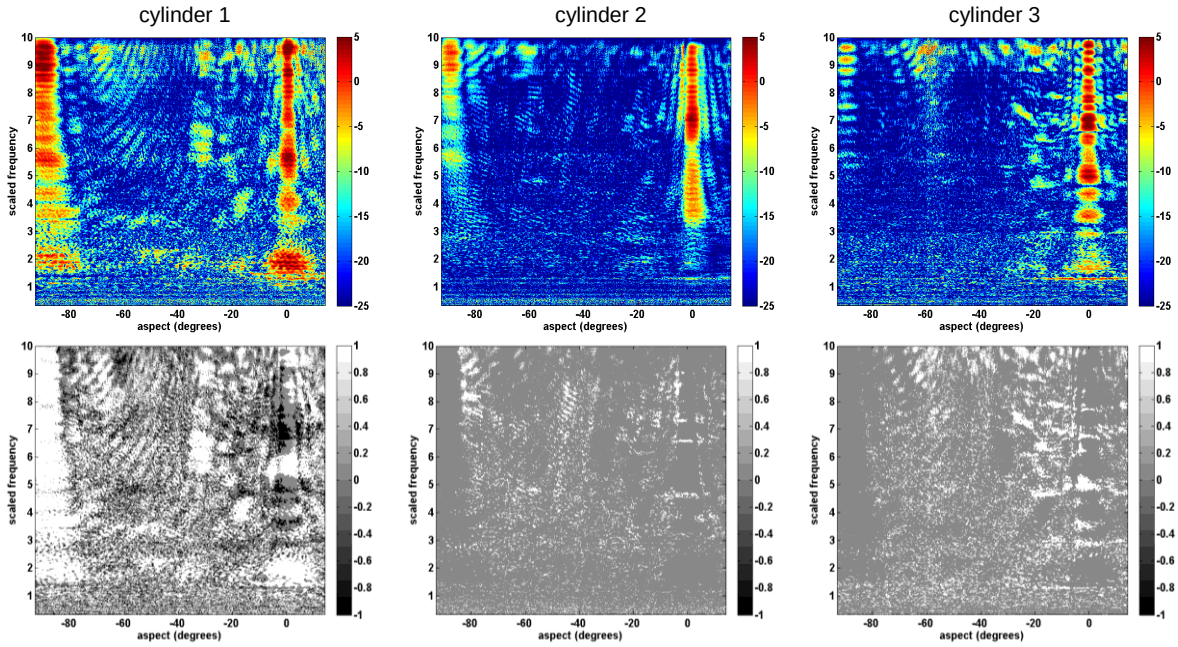


**Figure 15. Among a set of 3 like- shaped cylinders, a feature selection tool is applied to look for phenomena in the acoustic color of each target (top row) that is unique to that target (white or black regions in the corresponding plot below).**

requirements if robust signatures can be identified for the desired targets. In this study, the excitation of elastic surface waves was used to distinguish between 4 2ft-long by 1ft-diameter cylinders of differing material construction. Data for this study were from high grazing angle ($45^o$ and $34^o$) backscatter measurements on these targets deployed proud on the bottom of the NSWC PCD pond. Acoustic color plots for the isolated targets exhibited quasi-periodic spectral enhancements over a range of aspect angles that are attributed to dispersive surface borne Rayleigh or Lamb-type elastic waves excited and traveling along a path that navigate around the cylinder until they reach an end, reflect, and then travel towards the other end of the cylinder while radiating back towards the source/receiver. This dynamics is illustrated in Fig. 16 for one of the cylinders studied constructed of solid Al. The spectral properties of the reradiation due to these elastic phenomena are unique to the material makeup of the structure so they should be useful for discrimination.

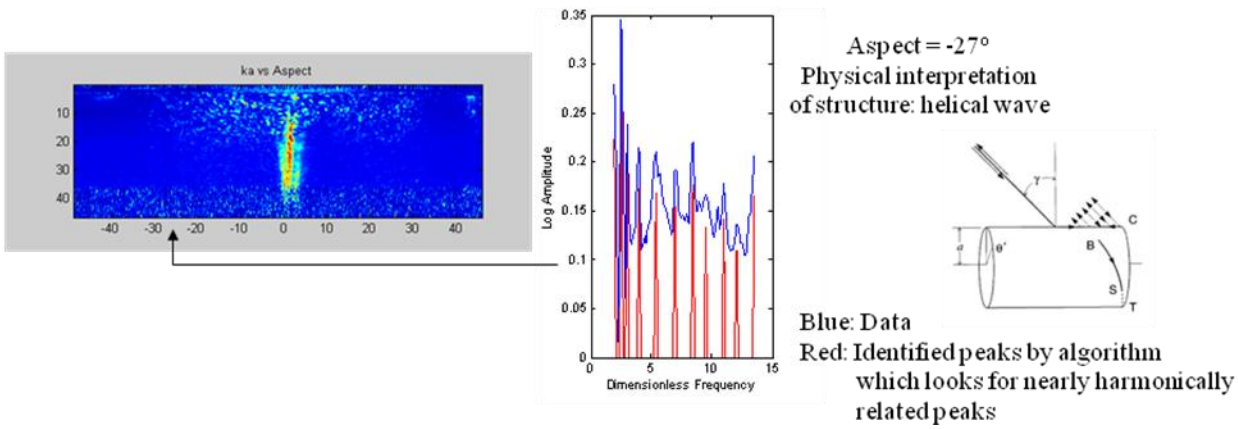


**Figure 16. Excitation of surface Rayleigh waves at -27$^o$ target aspect on a solid Al cylinder produces quasi-periodic structure in its acoustic color plot.**

To make use of these phenomena, features associated with them need to be extracted. This was done by selecting aspects from the acoustic color plots that exhibited spectral peaks with a certain spacing consistent with the acoustic coupling angle and surface propagation path and that also exhibited a specified minimum number and magnitude relative to the background. The associated pings for the 4 targets were then inspected by an algorithm that creates feature vectors consisting of a user selected list of values. For the present study, 5 elements were extracted: number of quasi-harmonic peaks, start frequency, separation between peaks, a salient factor (value dependent on relative size of peaks relative to the background), and aspect angle. These 5-element feature vectors from each target were fed into a K-means clustering algorithm, which can group the vectors into N clusters where N is a value that can be set to the number of different targets if this is known or a value iterated in a loop to determine the best clustering if the number of different targets is not known. This process is illustrated in Fig. 17. By setting N=4 for this initial study, the discriminatory power of the selected features was determined to be good since each cluster contained vectors for one target only. Furthermore, as shown in Fig. 18, a MATLAB generated silhouette plot for the clusters demonstrated good confidence in the assignments for the vectors in each cluster. The silhouette value for each feature vector is a

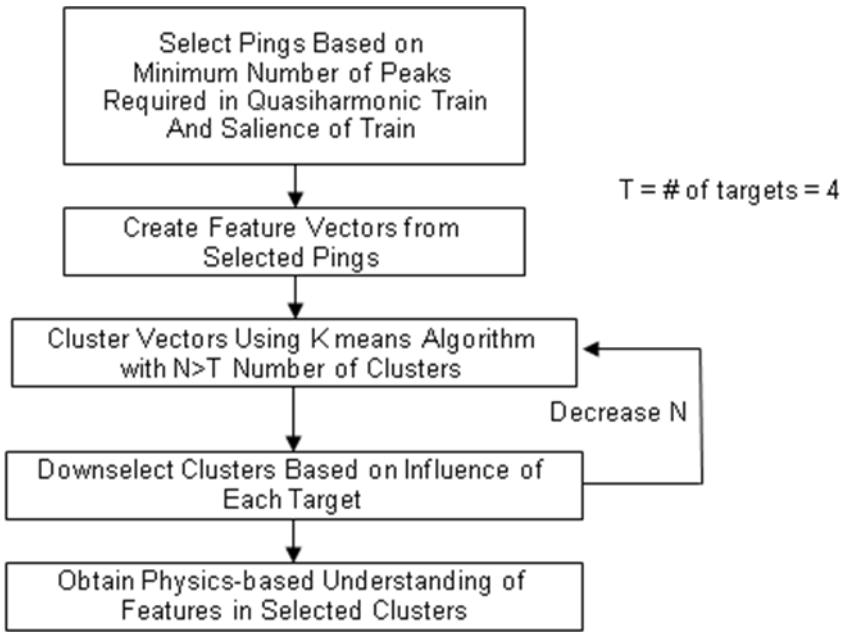


**Figure 17. Process for using elastic information in sonar data to discriminate between 4 cylindrical targets with the same size and shape.**

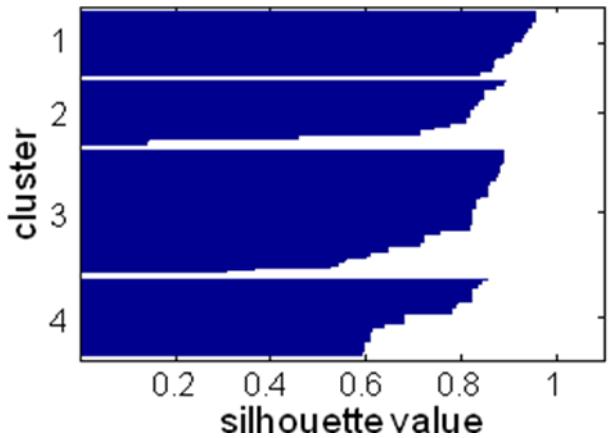


**Figure 18. Silhouette plot of four clusters in 5 dimensional feature space.**

measure of how similar that vector is to those in its own cluster compared to vectors in other clusters. Values range from -1 to +1 with high values indicating similarity within a cluster.

Of course, despite the good results, a caveat to this study is that it is based on a limited amount of data collected under conditions that allowed good SNRs on the targets included. Further study with data collected under more difficult conditions and/or more realistic shapes is needed. The effect of different feature vectors that include more peak related information (e.g., trends in peak heights and variability in peak spacing) can also be tried to improve classification performance if needed.

## Conclusions to date

Work performed under SERDP project MM-1666 continues to work towards a high fidelity simulation capability that can be used to test overall performance of new sonar designs operated under realistic conditions. However, detection and classification of more problematic UXO (e.g., those that are small and difficult to image) will likely need additional processing tools beyond sonar imaging to be effective. To deal with these UXO, ways to predict the performance of sonar configurations that extract more information from target responses and capture these responses in ways that yield higher SNR must be considered. Concepts currently being explored are increasingly making use of projections of target sonar responses onto non-imaging spaces that don't require high spatial resolution to determine what the target is. Furthermore, the target responses themselves are not being limited to backscatter since higher SNR is possible in bistatic detection configurations. Predicting performance under these conditions is based on the use of tools such as statistical classification algorithms that require a large amount of data to train and test with. Otherwise, misleading, often overly optimistic, results can be produced.

Many of the efforts carried out to date have focused on ways to enhance existing target response databases for physical analysis and testing and training of classification tools. This included continued collection and processing of target data on several UXO and clutter in NSWC PCD's pond facility and creating a capability to calculate target responses with FE. A long-term goal will be to supplement UXO sonar response measurements with accurate FE simulations so this capability has been developed in a systematic manner, with comprehensive verification and validation studies to ensure sufficient efficiency, speed, accuracy, and ease-of-use can be achieved. The FE capability at NSWC PCD is reaching sufficient maturity to carry out simulations for targets of realistic complexity. A near-term goal is to produce production level simulations of acoustic color plots for an empty, flat-end-capped cylindrical shell and then the 100mm projectile in Fig. 2 in a sand bottom.

Software tools were also developed to imbed target responses into realistic environments using PC SWAT and to increase the efficiency of data collection, processing of target representation schemes, and target classification. These tools have been used to supplement the data available but, because some simplifying approximations were made in implementing these tools, they will continue to be studied as needed to fully assess their impact. Nevertheless, their value for increasing classifier effectiveness is expected to be significant when compared to the expense of field surveys for providing the data otherwise required.

In upcoming work, the efforts performed so far will continue to expand and improve our understanding of the physics useful for classification. Initial studies using sonar-derived features based on physics unique to a target's composition has shown good performance in being able to remotely separate four cylindrical targets of the same size but different material construction when deployed on a sand bottom. This might be relevant to discriminating live from practice UXO rounds. While the features chosen were only used with a limited dataset, the potential for mitigating some of the training requirements of purely statistical approaches is clear. Physics can be used to identify phenomena to derive features from that are less sensitive to environmental effects. If environmental effects cannot be avoided, it may still be more efficient

to tune a classifier using physics to predict the effect on the features used than to collect more data for further training.

In addition, further classification analysis based on non-imaging target representations will be emphasized as this project goes forth. APL-UW (K. Williams) has written a MATLAB routine for accessing much of the 2010 pond data, including the software for isolating targets (T. Marston) and generating acoustic color plots, so that features can be derived from them and input into classifiers. This has been given to NSWC PCD classification specialists to facilitate use of the UXO data in their ATR algorithms.

## References

[1] M. Soumekh, **Synthetic Aperture Radar Signal Processing: with MATLAB Algorithms**, John Wiley & Sons, 1999.

[2] K. L. Williams, S. G. Kargl, E. I. Thorsos, D. S. Burnett, J. L. Lopes, M. Zampolli, P. L. Marston, "Acoustic scattering from a solid aluminum cylinder in contact with a sand sediment: measurements, modeling, and interpretation," *J. Acoust. Soc. Am.* **127**(6), 3356-71, 2010.

[3] S. G. Kargl, K. L. Williams, T. M. Marston, J. L. Kennedy, and J. L. Lopes, "Acoustic Response of Unexploded Ordnance (UXO) and Cylindrical Targets," Proceedings of MTS/IEEE Oceans 2010, Seattle, WA, Sept. 20-23, 2010.

# APPENDIX

# Acoustic scattering from a solid aluminum cylinder in contact with a sand sediment: Measurements, modeling, and interpretation

Kevin L. Williams, Steven G. Kargl, and Eric I. Thorsos
*Applied Physics Laboratory, College of Ocean and Fishery Sciences, University of Washington, Seattle, Washington 98105*

David S. Burnett and Joseph L. Lopes
*Naval Surface Warfare Center, Panama City Division, Panama City, Florida 32407*

Mario Zampolli[a)]
*TNO Defense, Security and Safety, Oude Waalsdorperweg 63, P.O. Box 96864, 2509 JG The Hague, The Netherlands*

Philip L. Marston
*Department of Physics and Astronomy, Washington State University, Pullman, Washington 99164*

(Received 14 December 2009; revised 5 April 2010; accepted 8 April 2010)

Understanding acoustic scattering from objects placed on the interface between two media requires incorporation of scattering off the interface. Here, this class of problems is studied in the particular context of a 61 cm long, 30.5 cm diameter solid aluminum cylinder placed on a flattened sand interface. Experimental results are presented for the monostatic scattering from this cylinder for azimuthal scattering angles from 0° to 90° and frequencies from 1 to 30 kHz. In addition, synthetic aperture sonar (SAS) processing is carried out. Next, details seen within these experimental results are explained using insight derived from physical acoustics. Subsequently, target strength results are compared to finite-element (FE) calculations. The simplest calculation assumes that the source and receiver are at infinity and uses the FE result for the cylinder in free space along with image cylinders for approximating the target/interface interaction. Then the effect of finite geometries and inclusion of a more complete Green's function for the target/interface interaction is examined. These first two calculations use the axial symmetry of the cylinder in carrying out the analysis. Finally, the results from a three dimensional FE analysis are presented and compared to both the experiment and the axially symmetric calculations. © *2010 Acoustical Society of America.*
[DOI: 10.1121/1.3419926]

PACS number(s): 43.30.Jx, 43.40.Fz [NPC] Pages: 3356–3371

## I. INTRODUCTION

Scattering from elastic objects placed on or near the water/sediment interface is a problem receiving increasing attention.[1–5] In many cases the targets of interest have been hollow spheres. This focus on spheres has been, in part, because numerical and analytical modeling of the target is well-developed; thus one can concentrate on the physics introduced by being near the sediment/water interface. However, recent developments in finite element (FE) modeling[4,6,7] now allow examination of more complicated elastic objects placed on the interface between two media.

In this article the target examined is a solid aluminum cylinder with flat ends. The cylinder is 61 cm long and 30.5 cm in diameter. It was placed on a flat sand/water interface (often called the "proud" target case, a terminology that will be used here) and data acquired at frequencies from 1 to 30 kHz over azimuthal angles from 0° (broadside) to 90°. Like the sphere, examination of scattering from finite elastic cylinders in the free field also has a long history from which the physical processes involved in the scattering can be quantitatively understood.[8–11] This insight is valuable for the present case when examining experimental results and when comparing FE modeling to these experimental results.

There are three goals in the present article. The first is to present experimental results for the absolute target strength of the proud cylinder as well as synthetic aperture sonar (SAS) images of the cylinder. These results are important for testing models not only within the rest of this article but hopefully also for models developed by other researchers. The second goal is to explain the experimental results within the context of previous physical acoustics analyses.[10,11] The final goal is to use data/FE model comparisons and the physical acoustics insights to better understand the essential physical processes and geometrical parameters that must be included in FE modeling in order to predict the absolute target strength of a proud cylinder for the geometries realized here.

The remainder of this article is organized as follows. Section II presents a summary of the experimental apparatus and procedure as well as the analyzed results. Section III

[a)]Part of the work presented was carried out while the author was at the NATO Undersea Research Centre, La Spezia, Italy.

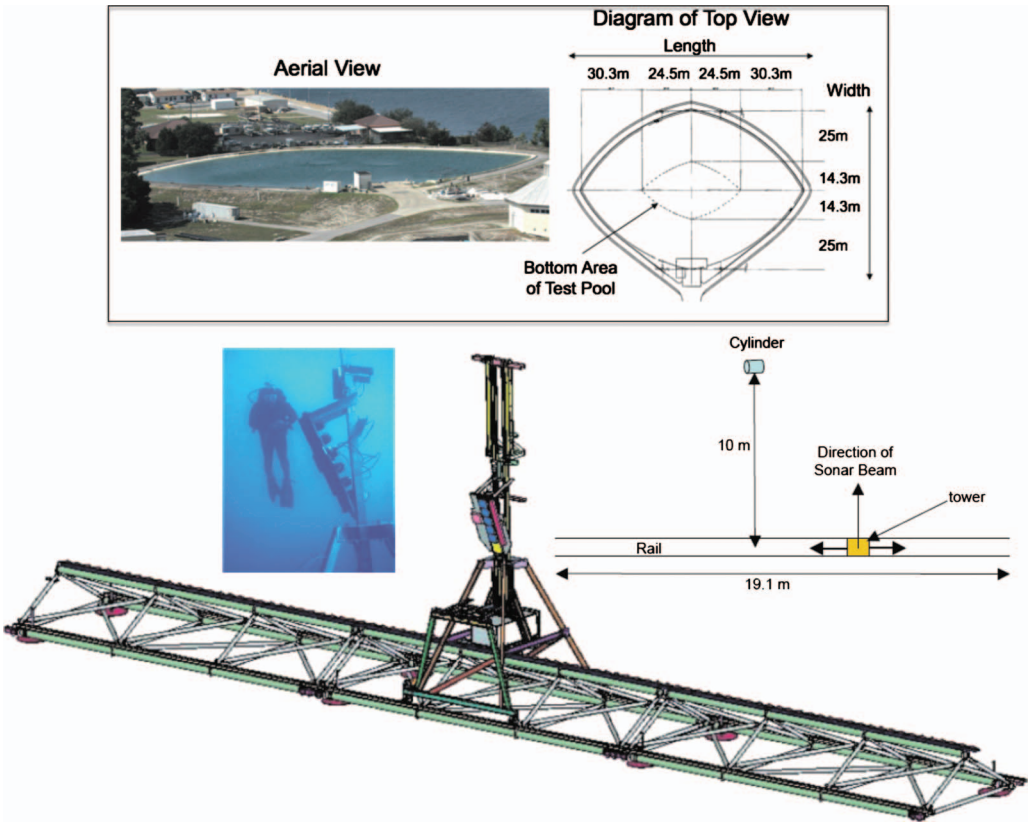


FIG. 1. Top: experiment facility. Bottom area identified in diagram is area covered by sand. Bottom: rail and mobile tower system used. The rail consisted of 3 rail sections each 7 m in length, resulting in a 19.1 m span over which the tower could be moved. Insert is a schematic of the experiment viewed from above, range to cylinder is approximate, see text for exact geometry. The underwater photograph includes side view of array used. The diver is in the background, the overall vertical extent of the array is approximately 1 m.

examines the experimental results using a process oriented view derived via physical acoustics. Section IV then describes a series of FE calculations with increasing fidelity relative to the actual experimental arrangement and the sediment/target interaction, and compares those results to the data. Section V summarizes. A subset of the author list concentrated on the work presented in particular sections. Section II documents the experiment and data analysis carried out by KLW, EIT, SGK, and JLL. Section III includes contributions from PLM, KLW, and EIT. Section IV A was written by DSB and Sec. IV B was written by DSB and MZ. Sections IV C–IV E were written by, and present the analyses of, KLW, MZ, and DSB, respectively.

## II. EXPERIMENT

The experiment described here was carried out in March 2008 in the Naval Surface Warfare Center test facility 383 in Panama City, Florida. The test facility includes a fresh water pool 110 m long by 80 m wide with 1.5 m of sand on the bottom. The water depth above the sand is approximately 14 m. The built-in filtration system allows 10 m dive visibility. The top of Fig. 1 shows both an aerial view and diagram of the facility.

### A. Apparatus and procedure

The measurement system used was designed to carry out backscattering measurements with sufficient spatial resolution to perform SAS imaging. The bottom of Fig. 1 shows an engineering drawing of the system. It comprises a bottom-mounted rail and a rail tower instrumented with transducers and position sensors. The rail is deployed by divers in sections, each rail section is 7 m in length. Rail sections are connected and leveled to form longer rail lengths; during the experiment 3 sections were used. The electric motor-driven tower traversed the rail at a constant speed of 5 cm/s. Transmissions were made twice per second as the tower moved along the rail; given the horizontal width of the receiver (10 cm) this transmission rate is sufficient for SAS processing.

The electronics controlling transmission, data acquisition and digitization, tower motion and monitoring of all position instrumentation (e.g., inclinometers, pressure sensors) resides in a tower-mounted electronics housing. Separate power and data/control cables are connected to this housing. These cables are attached to a triangle shaped guide at the backside of the tower to assure that the cables are not pinched as the tower moves. These cables were fed back to a mobile office where topside experimental control resided. Thus, data analysis could be carried out as the experiment proceeded and experiments altered based on those results.

The transmitted pulse used was a 6 ms FM slide from 1 to 30 kHz. The beamwidth of the transmitter is broad over the entire frequency range (full width greater than 40°) in order to allow SAS processing. The receiver contains six separate elements arranged in a vertical array, and each receive element has a 10 cm horizontal aperture. The vertical

apertures are (from top to bottom) 30, 10, 10, 10, 10, and 30 cm. Backscattering signals received on each element are recorded separately. This allows the vertical beam pattern to be altered to minimize scattering interference from the water/air boundary. It also allows time delay between separated receiver elements to be used to determine the depression angle of target returns relative to the center of the receive beampattern. Both source and receiver were calibrated as a function of frequency before the experiment to allow backscattered pressure to be determined in absolute units of dB re 1 $\mu$Pa with an uncertainty of approximately $\pm 1$ dB.

The transmitter and receiver are mounted on a panel and are separated horizontally by about half a meter. The panel can be rotated up or down in 5° increments. For the measurements presented here the inclinometer mounted on this panel indicated a tilt angle of 20.3° relative to the vertical. This angle plus the arrival time of the specular reflection from the cylinder to the receive elements allowed the geometry to be determined to an uncertainty of approximately 5 cm. At the point of closest approach, the horizontal distance from the center of the transmitter (receiver array) to the center of the cylinder (deployment discussed below) was 9.55 (9.45) m. The center of the transmitter (receive array) was 3.60 m (3.85 m) above the center of the cylinder. From these measurements the grazing angle for the ray drawn from transmitter (receive array) center to cylinder center was 20.7° (22.2°).

The aluminum cylinder was deployed by divers approximately 10 m from the center of the rail. Before deployment of the cylinder, the sand in a 3 m (range) by 2 m (cross range) area was flattened by divers using two I-beams deployed in the sand and a third I-beam used as a scrapper. After this operation the I-beams were removed and the cylinder deployed using a lift system that consists of a flotation bladder and built-in winch with wireless electronic control from shore. This system, along with an underwater communication system between divers and winch operator, allowed divers to remain neutrally buoyant above the flattened area while placing the cylinder at the designated location and orientation. Small lift lines from which the cylinder was suspended were removed, leaving only a small indentation (1 to 2 cm long and a few millimeters deep at two locations along the cylinder). The results shown here are from four deployments with associated orientations of the center line of the cylinder relative to the path of the rail tower of 0° (broadside), 25°, 47°, and 70°. For each cylinder orientation the tower traversed the entire length of the rail transmitting 800 times. The path of the tower along the rail defines the $y$ axis of the coordinate system used, with $y=0$ at the center of the rail. The azimuthal angle $\phi(y)$ (measured on the horizontal plane of the water/sediment interface) between a line from the tower (at any position $y$ along the rail) to the center of the cylinder and a line through the center of the cylinder that is in the horizontal plane and perpendicular to the cylinder axis will be an important parameter in the analysis that follows. It is useful to note that the orientations given above define $\phi(y=0)$ for each cylinder deployment.

The sound speed in the (fresh) water was determined from its temperature to be 1486 m/s. Based on the water temperature, the water density was 998.2 $\mathrm{kg/m^3}$. Two diver cores gave sediment densities of 1990 $\mathrm{kg/m^3}$ and 2020 $\mathrm{kg/m^3}$. For the simulations these densities were taken for water (sand) as 1000 (2000) $\mathrm{kg/m^3}$. The sound speed in the sediment, measured using a diver deployable measurement system,[12] was 1694 m/s. (These relative sediment/water speeds give a critical angle of 28.7°.) This same system enables sediment attenuation (given here in terms of $\delta_P$, the ratio of the imaginary to real wavenumber[13]) to be determined. $\delta_P$ was 0.008. Finally, the material parameters used for the aluminum cylinder were density=2700 $\mathrm{kg/m^3}$, longitudinal sound speed=6568 m/s, and shear speed =3149 m/s. Radiation damping dominates inherent attenuation for the waves within the cylinder that lead to measurable backscatter, and the FE results to be presented are thus not sensitive to attenuation values chosen; however, for completeness, the results shown here assumed 0.000 15 dB/m/kHz for the longitudinal wave and 0.000 3 dB/m/kHz for the shear wave.

### B. Results

Figure 2 presents the backscattering from the proud cylinder for the four different orientations. The pulse compressed backscattering levels were obtained by matched-filtering with the incident pulse. The scale is in dB relative to the brightest pixel in each panel. There is a rich structure of returns for all orientations. One goal in the remainder of the article is to understand this structure and to quantitatively compare FE modeling results to the data. In this regard, further analysis of these data will be useful. But first, two additional remarks on the broadside return in Fig. 2(a) can be mentioned here. The weak features at a time of about 13.5 ms preceding the main returns are side lobe artifacts from the matched filtering. The slight tilt away from vertical in the main returns [and later in the corresponding SAS image in Fig. 3(a)] arises because the divers were not able to position the cylinder exactly parallel to the rail in this case.

The data were SAS processed[14] to obtain the images shown in Fig. 3. The SAS processing (which ignores the horizontal offset between source and receiver) gives good focusing without further auto focusing efforts. The four panels coincide with the same panels in Fig. 2. The dB scale is again relative to the brightest pixel in each panel. The broadside SAS image [Fig. 3(a)] clearly indicates the length of the cylinder. The obvious multiple return structure in Fig. 3(a) as well as other features seen in panels of Figs. 2 and 3 and in Fig. 4(a) below will be identified in Sec. III.

The data were also processed to get absolute levels for the target strength of the proud cylinder as a function of azimuthal angle and frequency. The normalizing pressure is the magnitude of the transmitted pressure as a function of frequency at the location of the center of the cylinder in the absence of both the cylinder and the sand (i.e., in the free field). The result is shown in Fig. 4(a). The azimuthal angle is measured on the horizontal plane through the axis of the cylinder relative to broadside. Thus 0° is broadside and 90° is end-on as seen by an observer 0.15 m above the water-sand interface (i.e., an observation point on the plane through

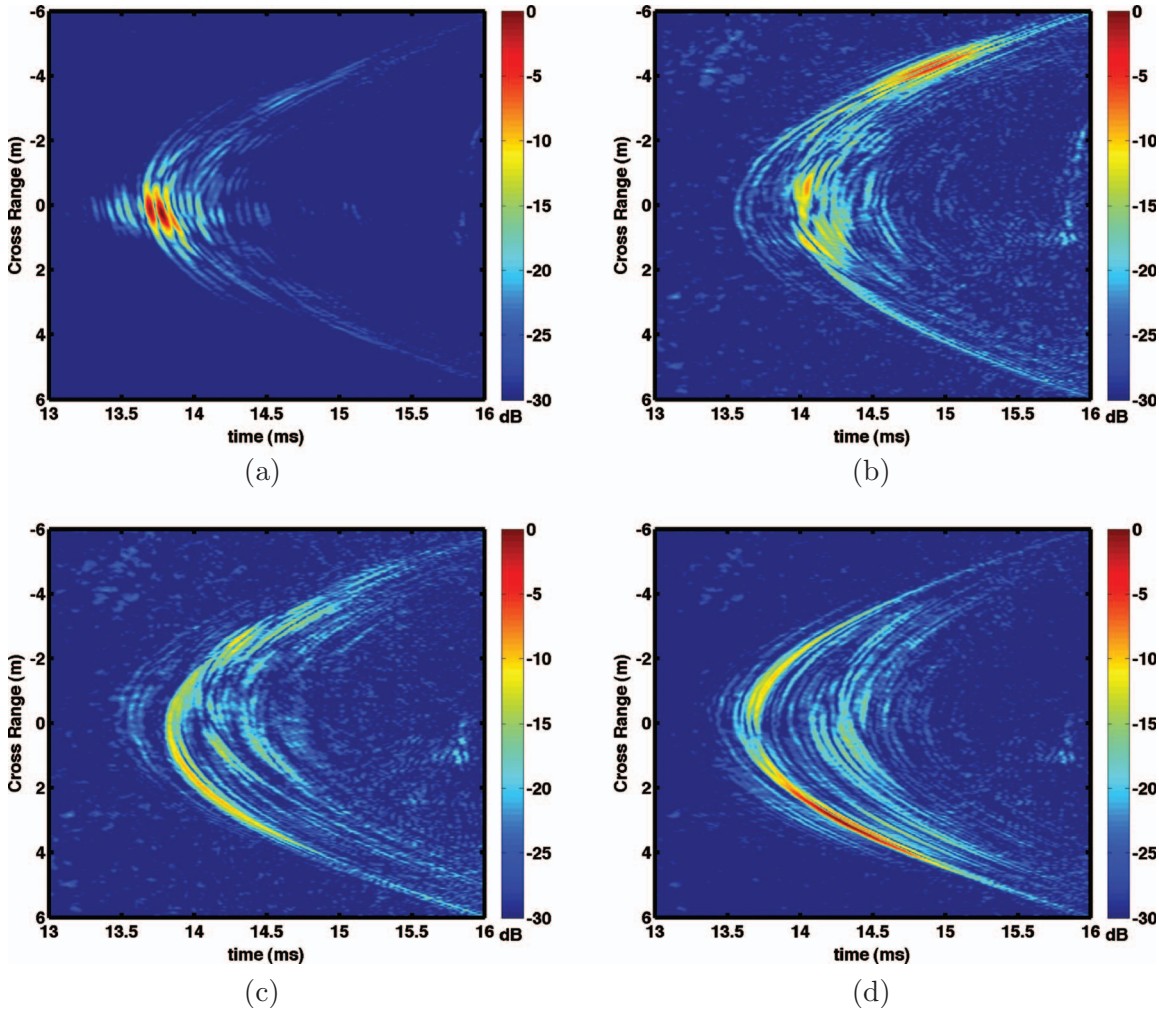


FIG. 2. Each panel shows pulse compressed and basebanded (i.e., signals downshifted by the center frequency) backscattering returns for a proud 60 cm long aluminum cylinder for 480 transmissions as the rail tower translated the central 12 m of the rail. The cylinder's orientation is different in each panel. The axis of the cylinder relative to the path of the rail tower for each case is (a) 0° (broadside), (b) 25°, (c) 47°, and (d) 70°. The dB scale is relative to the brightest pixel in each panel.

the center of the cylinder and parallel to the sand/water interface). Figure 4(a) was made using data in each panel of Fig. 2 within the cross ranges of about −2.5 to 2.5 m. Each orientation given in Fig. 2, and identified previously with $\phi(y=0)$, gives a center $\phi$ around which the target strength was determined for at most 20° on either side. The total $\phi$ range from broadside to end-on was obtained by combining the data from the four orientations. Note that the signal to noise ratio (SNR) of the data is lower in the 1–5 kHz region due to a decrease in transducer directivity. This reduced SNR is especially evident away from broadside.

Figures 4(b)–4(f) are results of FE calculations using different assumptions. They will be discussed in detail in the later sections but are grouped together with the experimental results to facilitate comparisons.

## III. PHYSICAL ACOUSTICS INTERPRETATION

The complications introduced by the proximity of the cylinder to the sediment are most easily seen in Figs. 2(a) and 3(a) where the broadside echo is split into a triplicate of features associated with paths discussed in Sec. IV C. That splitting is consistent with a ray analysis of reflections from cylinders and a flat adjacent surface given by Baik and Marston.[15,16] Geometrical considerations also identify echoes in Fig. 2(b) at a cross range of about −4.4 m and time of 15 ms and in Fig. 2(d) at a cross range of about 3.5 m and time of 14.3 ms as reflections from the side and end of the cylinder respectively. For these latter two cases additional physics (i.e., the additional echoes in those figures) complicates interpretation of the SAS images in Fig. 3.

The interpretation, given here, of some of this additional physics is most appropriate for $ka>10$ ($k$ is the acoustic wave number in the water and $a$ is the cylinder radius). Additional understanding and analysis related to lower $ka$ features can be found in the Ph.D. thesis of Baik.[15]

In the present case $ka>10$ translates to frequencies above 16 kHz. At these $ka$'s it is helpful to consider coupling conditions for the free field excitation of elastic waves guided by the surface of the cylinder.[10,11] Prior calculations of the phase velocity of high-frequency modes propagating down infinitely-long solid steel cylinders in water give values close to the speed of a Rayleigh wave on an elastic half space.[17] Calculations for an infinitely-long aluminum cylinder yield a similar result.[15] A noteworthy difference between

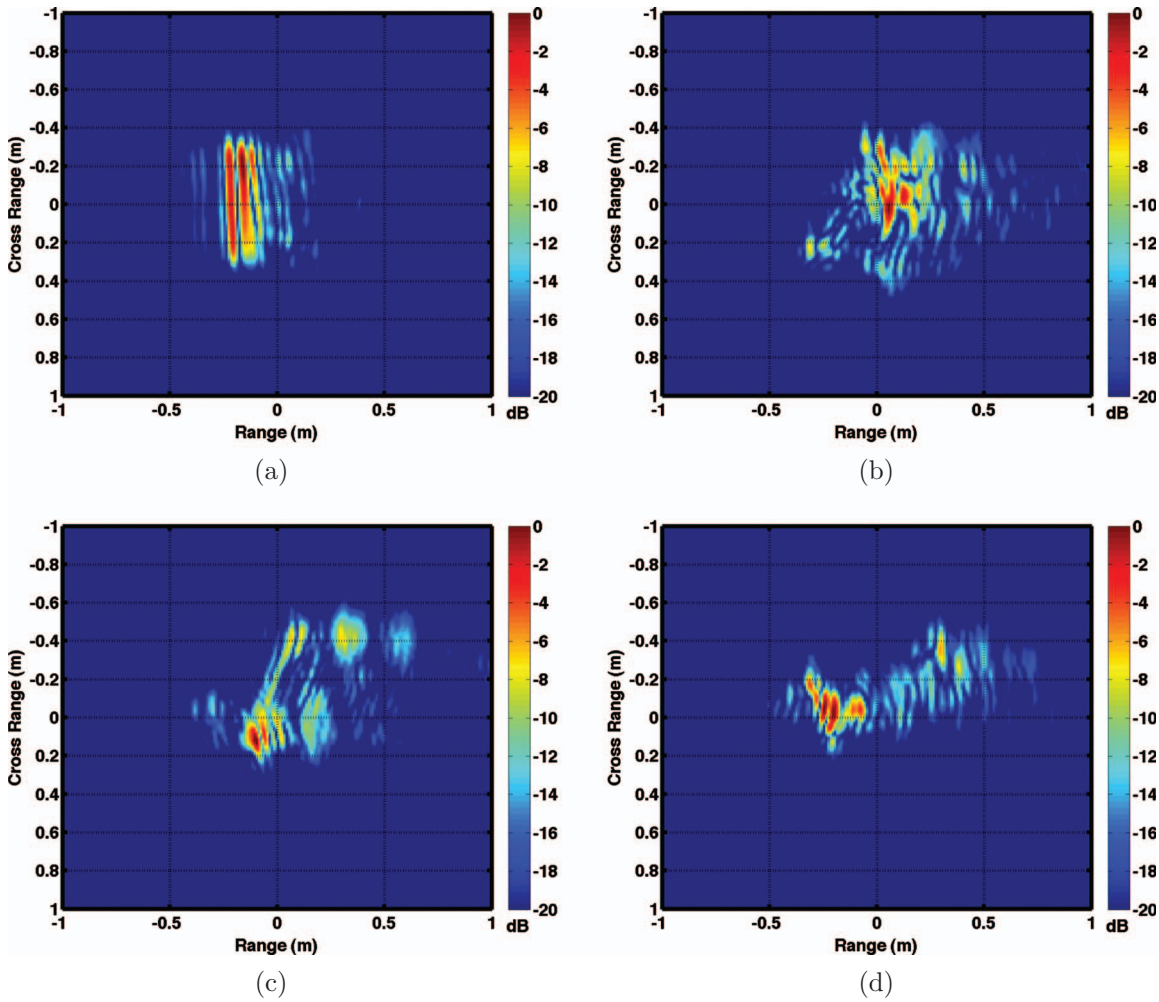


FIG. 3. The SAS images of the proud 60 cm long cylinder resulting from processing the data presented in Fig. 2. The dB scale is relative to the brightest pixel in each panel. Note that range 0 in the figure is relative to 9.5 m—the nominal horizontal distance from transmitter/receiver array to the center of the cylinder.

aluminum and steel cylinders is that the rates of radiation damping for most axially propagating modes on aluminum cylinders are over twice that for similar modes on steel cylinders as a consequence of the lower density of the aluminum.[18] This increase in radiation damping broadens the range of cylinder tilt angles over which the modes are excited.[15,18]

For the purpose of describing the coupling, it is convenient to consider free field ensonification by a plane wave having a wave vector $\boldsymbol{k}_i$. The plane containing the unit vector $\hat{\boldsymbol{k}}_i$ and a unit vector along the cylinder's axis $\hat{z}_{cyl}$ intersects the side of the cylinder closest to the source along a meridian of the cylinder. The excitation of high-frequency elastic waves propagating along the meridian is governed by the value of the tilt angle[10,17] $\gamma = \arcsin(\hat{\boldsymbol{k}}_i \cdot \hat{z}_{cyl})$ relative to the Rayleigh wave coupling angle $\gamma_R = \arcsin(c/c_R)$ where $c$ is the speed of sound in water and $c_R$ is the Rayleigh wave velocity. For aluminum in water $\gamma_R \approx 30°$. Experiments with metal cylinders having flat ends show that the backscattering is enhanced when $\gamma$ is close to $\gamma_R$ as a consequence of radiation associated with elastic meridional rays which have reflected off the end of the cylinder.[10,15] When $\gamma$ is decreased below $\gamma_R$, sufficiently long cylinders display backscattering features associated with the excitation and reflection of helical rays by the end of the cylinder.[9–11,15,19] Reflection from an adjacent flat surface reduces the length of cylinder required geometrically to give helical wave contributions to the backscattering (further comment on why this is the case is given at the end of the summary).

To compare the expected high-frequency behavior with features visible in Figs. 2–4, notice that $\gamma$ is related to the grazing angle $\theta_g$ (21.5° is used here for $y=0$ and in Sec. IV C below, this is the mean of the transmitter and receiver grazing angles) and the cylinder's azimuthal orientation angle $\phi$ by $\gamma = \arcsin(\cos\theta_g \sin\phi)$. See Eq. (A6) in the Appendix.

In Figs. 2(b) and 3(b), $\phi(y=0)$ is 25° so that $\gamma$ is 23° at cross range of zero. There are associated late echoes in Fig. 2(b) at cross range near zero and times after 14 ms. In Fig. 3(b) the back end of the cylinder appears bright (i.e., the complex structure at a cross range from about −0.4 to 0.1 m and a range of about 0.1 to 0.2 m). The late arrivals in Fig. 2(b) and the enhancement of the back end of the cylinder in Fig. 3(b) are due to the radiation characteristics of meridional and helical waves. Some of the complicated structure is hypothesized as due to the combination of this elastic contribution and the reflection from the side of the cylinder discussed earlier.

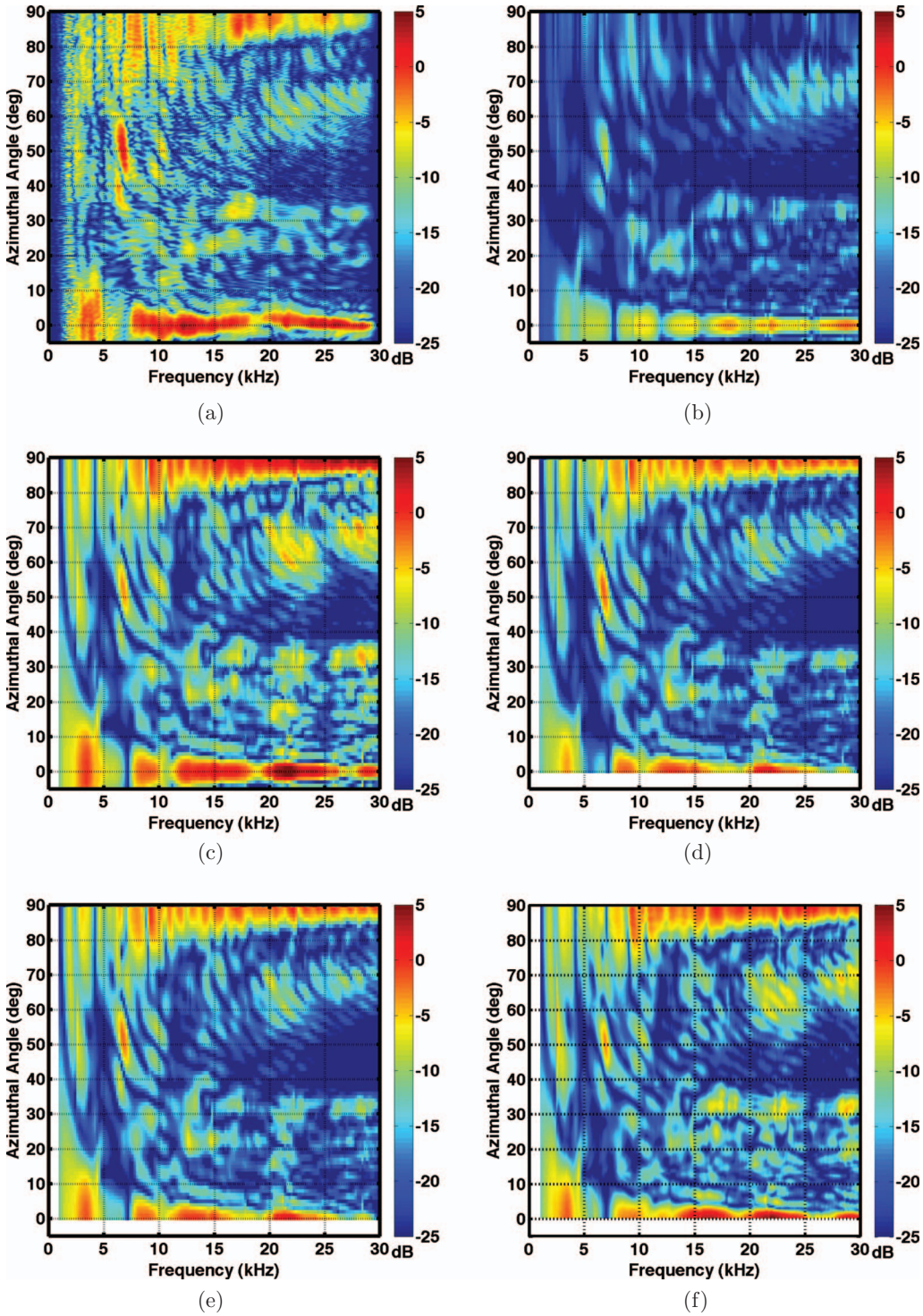


FIG. 4. (a) shows the experimental result for the absolute target strength of the proud cylinder as a function of azimuthal angle and frequency. (Note that 0° is broadside and 90° is azimuthally end-on but still at a vertical angle of about 21.5° to the center of the cylinder.) The other subplots show FE results, all but the last use axial symmetry and 2-D FE: (b) absolute target strength of the free field cylinder as a function of azimuthal angle and frequency calculated assuming source and receiver at infinity; (c) absolute target strength of the proud cylinder as a function of azimuthal angle and frequency calculated assuming source and receiver at infinity and using image cylinders to account for cylinder/interface interactions; (d) absolute target strength of the proud cylinder calculated using actual experiment geometry and with second order accurate layered medium Green's functions; (e) absolute target strength of the proud cylinder calculated using actual experiment geometry and with first order accurate layered medium Green's functions; (f) 3-D FE computation of absolute target strength of the proud cylinder as a function of azimuthal angle and frequency.

In Figs. 2(c) and 3(c), $\phi(y=0)$ is 47° so that $\gamma$ is 43°. The aforementioned backscattering enhancements are suppressed and the magnitude of the scattering associated with the far end of the cylinder is greatly reduced near $y=0$. However, $\phi(y=3\ \text{m})$ [a region where a bright arc is seen in Fig. 2(c)] is approximately 64.5° so that $\gamma$ is 57°. This $\gamma$ is close to the predicted value of $90°-\gamma_R \approx 60°$ associated with the excitation of a face-crossing Rayleigh wave on the flat near end of the cylinder.[11] When the excited wave reflects from the curved edge of the cylinder, the radiation from the re-

flected Rayleigh wave is directed toward the source of the sound. In agreement with that interpretation the end of the tilted cylinder closest to the source appears brightest in Fig. 3(c). Near $y=-3$ m in Fig. 2(c) $\gamma$ is close to 30° and the bright feature near 14.4 ms appears to be a meridional wave feature which brightens the back end of the cylinder in Fig. 3(c) (cf., at a cross range of −0.4 m and range of about 0.3 m).

In Figs. 2(d) and 3(d), $\phi(y=-1\ \text{m})$ is 64° so that $\gamma$ is again near 57°. This $\gamma$ is again close to the predicted value of $90°-\gamma_R \approx 60°$ associated with the excitation of a face-crossing Rayleigh wave on the near flat end of the cylinder.[11] The end of the tilted cylinder closest to the source again appears brightest in Fig. 3(d), however the structure in both Figs. 2(d) and 3(d) is complicated by combination of this elastic contribution and the reflection from the end of the cylinder.

The interpretations in the previous paragraphs are also complicated by the fact that images naturally include contributions from elastic effects below $ka=10$. Figure 4(a) allows separation of these lower frequency contributions. The elastic features discussed can then be viewed within the high frequency structure in Fig. 4 where the vertical axis gives the cylinder's apparent azimuthal orientation angle $\phi$. The face-crossing enhancement (near $\phi=60°$) is most noticeable above 19 kHz ($ka \approx 12$), which is consistent with free field observations for steel[11] and aluminum[15] cylinders. Between the face-crossing and meridional-ray enhancements the high frequency scattering is weak. The meridional-ray feature near $\phi \approx 32°$ ($\gamma \approx 30°$) is suppressed below 15 kHz. The features are also visible in the FE results discussed in Sec. IV.

There are also enhancements below $ka=10$ (16 kHz). Some of these are associated with the coupling of sound with specific resonances of the truncated cylinder. A noticeable example is the feature near $\phi=50°$ and 7 kHz in Fig. 4(a). It is the combination of this response and the face crossing response that we hypothesize leads to a bias below 60° of the face crossing features discussed in relation to Figs. 2 and 3. The detailed features associated with narrow spectral contributions such as the one near 7 kHz in Fig. 4(a) are not easily described for Figs. 2 and 3.

## IV. FINITE ELEMENT MODELING

Finite element (FE) modeling of the proud cylinder's target strength is presented within this section. Two fundamentally different FE formulations are used: a fully 3-D code and a hybrid 2-D/3-D code. Section IV A describes the mathematical problem that both codes seek to solve and Sec. IV B explains the essential differences in how the two codes go about this. These two sections provide an introduction to more detailed descriptions in Secs. IV C–IV E. In particular, Secs. IV C and IV D describe two different levels of physics approximation using the hybrid 2-D/3-D code and Sec. IV E describes the fully 3-D code, which analyzes the governing 3-D partial differential equations (PDEs) directly, without any further physics approximations.

### A. The mathematical problem

The idealized mathematical problem analyzed by both codes is steady-state acoustic scattering from a solid elastic cylinder immersed in two fluid half-spaces. The governing PDE in the cylinder is the linear elastodynamic equation for viscoelastic, anisotropic, inhomogeneous solids,

$$-\nabla \cdot (\mathbf{c}\,\nabla\,\mathbf{u}) - \omega^2 \rho_s \mathbf{u} = 0, \tag{1}$$

where $\mathbf{u}$ is particle displacement, $\mathbf{c}$ is a 4th-rank tensor of elastic moduli and $\rho_s$ is solid density. The governing PDE in the fluids is the linear Helmholtz equation for inviscid (though including bulk attenuation), anisotropic, inhomogeneous fluids,

$$-\nabla \cdot \left( \frac{1}{\omega^2 \rho_f} \nabla p \right) - \frac{1}{B} p = 0, \tag{2}$$

where $p$ is the scattered acoustic pressure, which satisfies the Sommerfeld radiation condition at infinity, $\rho_f$ is fluid density and $B$ is bulk modulus. The incident field is either a plane wave or the field produced by a monopole at a prescribed location.

Mathematically, this is a well-posed problem for which there exists a unique solution. If a solution is sought using a discretization method, e.g., FE analysis, then a small modification to the physics must be made: The infinite half-spaces must be truncated to finite spaces with outer fluid boundaries close to the object, typically one or two wavelengths away. Doing this, the FE domain is then reduced to the cylinder immersed in a small volume of fluid(s). This modification, in turn, requires two additional relations to be added to the mathematical problem:

(i) The Sommerfeld radiation condition at infinity must be replaced by non-reflecting and/or absorbing conditions imposed on or inside the outer boundary. The fully 3-D code uses the Bayliss-Gunzburger-Turkel (BGT) 2nd-order boundary condition.[20] The hybrid 2-D/3-D code[4,6] uses a "perfectly matched layer" (PML). Both approaches introduce a very small and controllable physics error, typically O(1%), often much less, which is insignificant relative to the model/data differences of several dB (many tens of percent) in this paper. Consequently, this issue is of no further relevance to the discussions in Sec. IV.

(ii) Since the fluid domain extends only a wavelength or two from the target, the scattered field is usually sought at locations well outside the FE domain. To accomplish this, both codes use the Helmholtz integral, which integrates the scattered field and the environmental Green's function over a closed surface circumscribing the target.[21] This integral incorporates the same physics as in Eq. (2), so no new physics errors are introduced. Consequently, as above, this issue is of no further relevance to the discussions in Sec. IV.

In summary, the essential differences between the two codes all pertain to how they deal with Eqs. (1) and (2). This is discussed in the next section.

## B. How the fully 3-D and hybrid 2-D/3-D codes treat the mathematical problem in Sec. IV A

### *1. Fully 3-D code*

Since this approach is *fully* 3-D, the modeling approach is straightforward: Eqs. (1) and (2) are *modeled directly*; i.e., the dependent variables **u** in Eq. (1) and $p$ in Eq. (2) are discretized, without making any additional physics or mathematics approximations. The FE analysis therefore solves Eqs. (1) and (2) directly for **u** and $p$.

No *a priori* knowledge of physical phenomenology (Sec. III) is necessary. Traditional methods for mesh convergence and error estimation, used routinely in industry for almost half a century, tell the modeler when an accurate and reliable solution has been achieved.

### *2. Hybrid 2-D/3-D code*

This code makes two physics approximations that simplify the mathematics in those cases where the overall geometry of target and sediment is not axially symmetric, such as in the present problem: (i) It ignores the presence of the sediment, in order to change the problem to a 2-D axisymmetric problem (the 2-D part of the hybrid approach), and (ii) then takes into account the effects of the sediment up to the first-order via reflection between the sediment and the source and the sediment and the cylinder (the 3-D part of the approach). Considering the target to be in the free field permits decomposing Eqs. (1) and (2) into an infinite number of 2-D Fourier azimuthal PDEs, whose solutions are Fourier modal amplitude functions which depend only on the cylindrical radial and elevation coordinates, but are independent of the azimuthal coordinate. The exact solution of Eqs. (1) and (2) would comprise an infinite number of Fourier modes, so the series is necessarily truncated at the finite number of modes at which the desired convergence of the free field solution has been achieved. A well known issue is that the decomposition of the problem into azimuthal Fourier modes is not always faster than the fully 3-D approach, depending on how many Fourier modes are needed to achieve a comparable accuracy. In the scattering formulation used here, the number of modes needed is determined by the number of terms which are necessary for the convergence of the incident field expansion into azimuthal Fourier modes (the closest integer larger than $1.6ka$ was used here[22]). For the plane and spherical incident wave fields used here, the number of modes required to obtain convergence is sufficiently small, so that the method is faster than a corresponding fully 3-D computation. The second advantage of the 2-D model is the reduced memory requirement compared to a corresponding fully 3-D model.

In the 3-D phase, the interaction with the water-sediment interface is treated by decomposing the incident field into a direct incident component and a boundary-reflected incident component, and by introducing an image cylinder below the water/sediment interface to treat the multiple rescattering between the cylinder and the interface to first order. This hybrid approach takes into account only first-order scattering between the scatterer and the seabed while the fully 3-D model takes into account all orders of scattering.

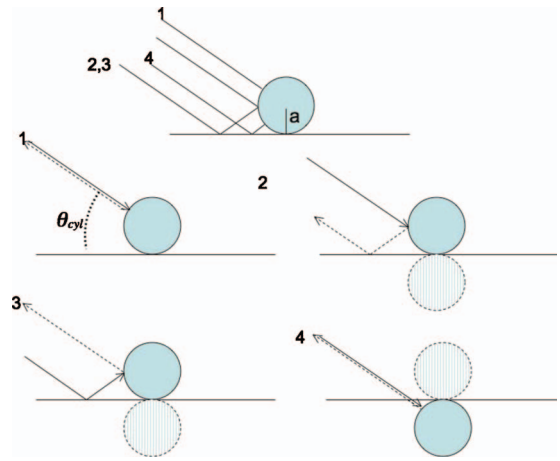


FIG. 5. Paths included in FE calculation in Sec. IV C. Top panel shows all paths and the bottom four panels show the separate paths. Paths 2 and 3 are reciprocal and include one bottom bounce, path 4 includes two bottom bounces.

A further limitation of the 2-D/3-D hybrid approach is that it cannot treat the fluid loading discontinuities which occur when the cylinder is partially immersed in the sediment, even only by a small fraction of the radius. These effects can be addressed only by the 3-D model. This may be relevant in connection with the differences between the 2-D models and the measurements, which are found in those regions of the angle-frequency space, where helical waves dominate the echo. (However, a final conclusion on this issue awaits further modeling comparisons where the geometries included are the same, e.g., later sections detail a difference in assumptions about the source-to-target geometry).

Sections IV C and IV D provide more details on the 2-D/3-D hybrid approach; Sec. IV E provides details on the fully 3-D approach.

## C. Hybrid 2-D/3-D code: First-order Green's function approximation; source/receiver at infinity

This most approximate FE calculation assumes the source and receiver are far enough away to use plane wave approximations, ignores the horizontal offset between source and receiver, uses the results calculated for the cylinder in the free field, and includes the effect of the interface via image cylinders. This allows the use of plane wave, FE results calculated using the axial symmetry of the cylinder in the free field. This can have a computational advantage since the free field result can be determined via multiple 2-D calculations instead of a full 3-D calculation. Figure 5 shows the paths taken into account and the image cylinders. The figure is oriented such that the observer is looking down the cylinder axis but the paths shown should be viewed as projections of the paths for any incident direction onto this plane. Several facts can be immediately discerned from the figure. First, the paths labeled 2 and 3 represent bistatic scattering paths even though the source and receiver are arranged in a monostatic geometry. Second, paths 2, 3 and 4 are delayed relative to path 1 in arriving to the receiver. The phase delay of paths 2 and 3 in arriving to the receiver relative to path 1 is $2ka \sin \theta_g$ and the delay of path 4 is $4ka \sin \theta_g$ ($k$ is

wavenumber, $a$ is the cylinder radius, and $\theta_g$ is the grazing angle onto the sediment) regardless of the azimuthal rotation of the cylinder relative to the acoustic path. However, the angle $\theta_{cyl}$ (which is the bistatic angle as measured in the cylinder coordinates) in Fig. 5 is equal to $\theta_g$ only when the cylinder is broadside to the acoustic path. For all other azimuthal orientations (angles $\phi$), $\theta_{cyl}$ can be defined in terms of $\theta_g$ and $\phi$. The Appendix presents the cylinder coordinates and angles $\phi_{cyl}$ and $\theta_{cyl}$ and derives expressions for them in terms of the relevant experiment angles $\theta_g$ and $\phi$.

The backscattering target strength to be presented here is calculated as

$$TS(f,\phi,\theta_g) = 20\log(r_r/(r_o P_o)(p_{path1} + 2R_{ws}(\theta_g) \times \exp(i2ka\sin\theta_g)p_{path2} + R_{ws}^2(\theta_g) \times \exp(i4ka\sin\theta_g)p_{path4})), \quad (3)$$

where $r_r$ is the range from the center of the cylinder to the receiver, $r_o$ is the reference range of 1 m, $R_{ws}(\theta_g)$ is the water/sediment reflection coefficient (in the present case the sand sediment was treated as a fluid), and $P_o$ is the incident pressure at the location of the cylinder in the absence of the sediment. The 2 in the path 2 term accounts also for the reciprocal path 3.

The FE calculation[6] to obtain the pressures for the paths in Eq. (3) is for the cylinder in the free field. The pressures $p_{path1}$ and $p_{path4}$ are taken as equal and are the backscattering pressures as a function of $\phi_{cyl}$ (with $\theta_{cyl}=0$). The calculation of $p_{path2}$ has to account for the bistatic nature of that path (and path 3) and the required bistatic angle is $2\theta_{cyl}$. Thus the path 2 contribution depends on both $\phi_{cyl}$ and $\theta_{cyl}$ which are functions of $\phi$ and $\theta_g$ given in the Appendix.

There are several assumptions implicit in this calculation. The use of a single grazing angle with parallel incident and scattered angles implies the source and receiver are far enough away to assume plane wave incidence and return. (Far field geometry is also implicit in the use of $r_r$ for all paths). It is assumed that the two-fluid Green's function[4] can be accurately approximated via use of a reflection coefficient. It also ignores any alteration of the target response due to the contact with the sediment and any multiple scattering between target and interface. These assumptions are tested in subsequent subsections.

The FE calculation used a mesh size of 2 cm. The convergence of the free field result using this mesh size was tested at the highest frequency of the calculation (30 kHz) for azimuthal angles from 0° to 90°. Calculations were done for mesh sizes of 4, 2 and 1 cm. Differences as large as 2 dB were found between the 4 and 2 cm meshes. The largest difference seen between the 2 and 1 cm results was 0.2 dB. The same mesh size was used for all frequencies. This certainly increased run time dramatically but allowed a "start and forget" approach. The run time to calculate TS every 200 Hz from 1 to 30 kHz and every 1° from 0° to 90° was about six days on a dual processor, 3 GHz computer.

Two results are presented. Both give absolute target strength to be compared to Fig. 4(a). Figure 4(b) shows the target strength for the cylinder in the free field. Figure 4(c) shows the target strength for the proud cylinder as calculated via Eq. (3) using a $\theta_g$ of 21.5° (the mean of the transmitter and receiver grazing angles).

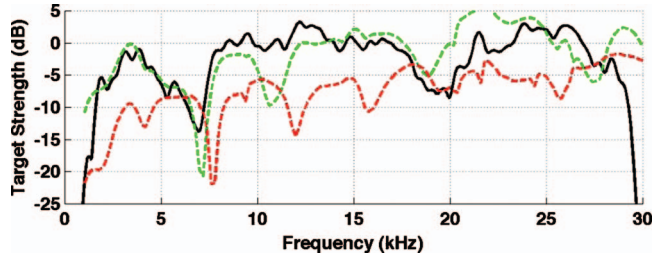


FIG. 6. Comparison broadside target strength: data (black), free field FE calculation (red), and proud FE calculation (green) using Eq. (3).

It is immediately obvious that the free field result does not match the overall target strength measured in the experiment as well as the proud result does. Closer examination also shows that much of the detailed structure seen in the experiment is reproduced in the proud FE calculation. However, there are also regions in frequency-$\phi$ space where there is significant discrepancy, e.g., for frequencies of 15 to 30 kHz with azimuthal angles from 10° to 20°. This particular region has been identified in the previous section as including contributions from helical waves that have the potential to be more significantly impacted by the fact the cylinder is on the sediment. The question to be examined next is to what extent more sophisticated FE calculations improve data/model comparisons.

Before proceeding, however, it is interesting to examine the broadside ($\phi=0°$) and $\phi=90°$ results further. Figure 6 compares data and FE results for broadside. Enhancements in target strength of up to 10 dB are seen in both the data and the proud FE results relative to the free field case. For $\phi=90°$ the free field result is much lower than the proud data and FE results because there is no scattering from the flat end back to the receiver. It is the single bounce paths from the end that gives the main contribution to scattering near $\phi=90°$.

### D. Hybrid 2-D/3-D code: Second-order Green's function approximation; source/receiver at a finite distance

In an attempt to address the discrepancies between the target scattering FE model results of Sec. IV C and the experimental data, the axisymmetric target scattering model is modified to include the source at a finite distance, and the vertical position of the receiver array element locations for the various positions along the rail. (It is important to note that here and in the next section on 3-D FE, the horizontal offset between source and receiver is still ignored, in part to allow comparison to the results of the previous section and also motivated by the fact that SAS processing gives good focusing when this offset is ignored). The source at a finite distance is modeled as a point source, which is decomposed into the azimuthal modal cosine series required by the axisymmetric target scattering model[6] using the fast Fourier transform. The procedure followed for taking into account the presence of the seabed is similar to the procedure repre-

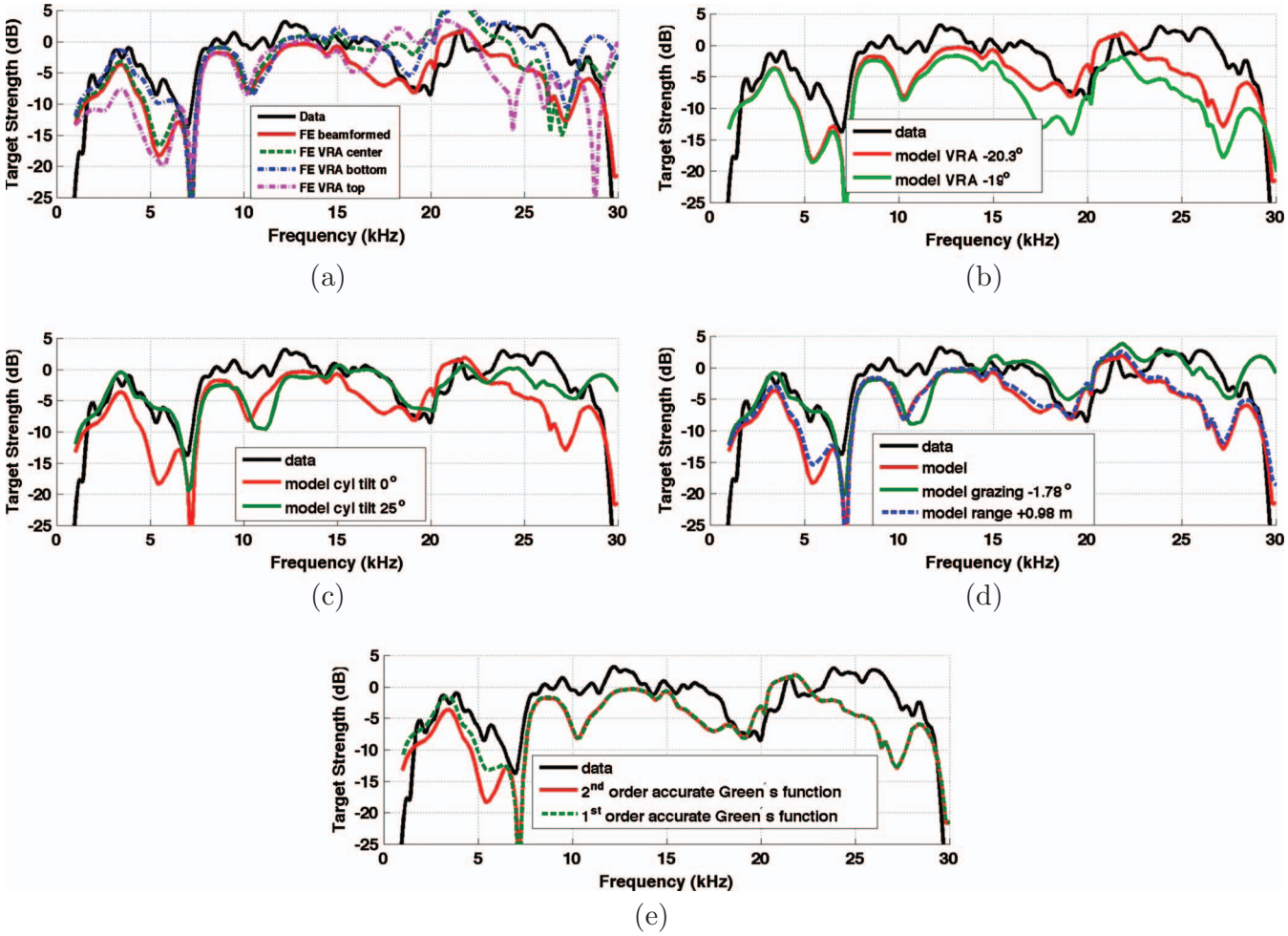


FIG. 7. (a) Target strength as a function of frequency at broadside aspect and cylinder orientation parallel to the rail, computed by taking into account the actual source-target-receiver geometry of the experiment. Strong variations of the target strength as a function of sensor location along the vertical receive array are evident. The red curve shows the effect of applying the beamforming to the model results. (b) Variation of the simulated beamformed array response caused by changes in the vertical receive array tilt angle. (c) Computed target strength for broadside insonification, obtained by two different combinations of cylinder orientation relative to the rail and tower displacement. (d) Sensitivity of the beamformed array response to changes in the grazing angle (keeping the range constant), and to changes in the range (keeping the grazing angle constant), for broadside insonification and cylinder orientation 0° with respect to the rail. (e) Computed target strength for broadside insonification, obtained using different approximations of the layered medium Green's function. The first order accurate Green's functions are equivalent to those used in Sec. IV C, however, the first order result here includes the actual experimental geometry instead of the assumption of plane wave incidence and scattering.

sented in Fig. 5, which takes into account the first order interactions between the incident field, the target, and the seabed, neglecting higher order multiple reflections and neglecting the impedance jump at the target/fluid interface in contact with the seabed.

For a given location and orientation angle of the cylinder with respect to the rail, one determines the actual positions of the source and of the receive array element centers and the resulting incidence angle on the cylinder in-plane with the sea floor. The FE computation is carried out for the signal incident directly from the source, and for the bottom reflected incident signal (image source contribution), which is multiplied by the sea floor reflection coefficient associated with the grazing angle of the ray connecting the image source and the target center. For each of the incident fields (source and image source contribution), the coordinate system is rotated into the coordinate system of the FE calculation, according to the Appendix, and the problem is solved with the FE model. In the final step, the result from each of the two FE calculations is translated back into the physical coordinate system, and the scattered field is repropagated from the target surface to the receivers using the discrete sum representation of Helmholtz integral with the approximate two-layered medium Green's function presented in Eqs. (4)–(6) of the work by Zampolli *et al.*[4] This yields two target echo components at the receiver locations, one generated by the source incident field and one generated by the boundary reflected incident field (image source), which are added up coherently at each receiver. In addition, for the beamformed results shown below, the complex pressures at the vertical receiving array elements (though with some tilt) are coherently summed.

Figure 7(a) shows the strong variability of the simulated target strength with receiver location, and the effect of beamforming the simulated responses at the receive array element centers. Even at the lower frequencies there are large variations between the echoes at the receiver locations along the vertical array, caused by the interference between the direct

and the boundary reflected echo components. Since it is beamformed data that are shown throughout the paper, in what follows below the simulated response at the array elements is beamformed by adding coherently the complex pressures computed at each of the hydrophone center locations.

The strong variability in the simulated echo, associated with small changes in the source-target-receiver geometry, is also evident in Fig. 7(b), which shows how a relatively minor change in the array tilt angle (just 1.3°) causes large changes in the computed target strength. Furthermore, a given source-target aspect angle can be obtained by changing the cylinder orientation, and by displacing the tower along the rail. Figure 7(c) shows a comparison between the simulated responses computed for broadside incidence with the cylinder parallel to the rail and the tower located at the center of the rail, and with a cylinder orientation of 25° relative to the rail and the tower displaced by 4.45 m with respect to the rail center. Also in this case it can be seen that the variations in the computed response associated with changes in the geometry are not negligible.

The difference between the broadside insonification ($\phi = 0°$) at 0° cylinder orientation and at 25° lies in the grazing angle, which decreases by 1.78°, and in the horizontal range between the target and the rail, which increases by 0.98 m. To address the effects associated with each of the two changes independently, the cylinder oriented at 0° with respect to the rail is considered, and two separate simulations are carried out: one in which the height of the source and receive array is changed so as to reproduce the change in grazing angle, and one in which the grazing angle is kept constant and the horizontal range, and consequently also the source and receive array height, are changed. Figure 7(d) shows the result of these computations in comparison with the broadside insonification case for the tower in the same position as the experiment, and in comparison with the data. The target strength appears to be sensitive mainly to small changes in the grazing angle. Figures 7(a)–7(c) suggest that the actual source-target-receiver geometry of the experiment should be taken into account by the numerical model. Nevertheless, some discrepancies such as the null near 10 kHz appear to be stable with respect to variations in the geometry.

In the examples of Figs. 7(a)–7(c), the Green's function used in the model is the second order accurate approximation resulting from the steepest descent approximation of the wavenumber spectral integral [Eqs. (4)–(6) in Zampolli *et al.*[4]]. In this approximation, the Green's function is described by a direct free field point source and an image point source premultiplied by an effective reflection coefficient that accounts for the spectra of plane waves contributing to the fields realized for finite source/receiver geometries. An additional lateral wave contribution, originating from a branch point contribution in the integrand of the spectral wavenumber representation, is also taken into account. The first order accurate approximation, instead, considers only the direct free field point source and the image source multiplied by the plane-wave reflection coefficient associated with the grazing angle of the ray connecting the image source and the source point of the Green's function. Figure 7(e) shows the comparison between the model results obtained by the FE model with second order accurate Green's functions, and by the same model using the first order accurate Green's functions. The two computed target strength curves are virtually identical across most of the frequency band, with the first order approximation exhibiting a better agreement with the experimental data at the lower frequencies. The first order accurate Green's function can be obtained from the second order accurate one by omitting the correction term in the reflection coefficient, $-iN/(kR_1)$ in Eq. (4) of Zampolli,[4] and by omitting the lateral wave contribution, Eq. (6) in that same reference. Eliminating the two terms one at a time, and performing the comparison between the numerical results obtained, shows that the second order correction to the reflection coefficient is negligible in the cases considered here, and that the lateral wave contribution does not appear to be visible in the experimental results.

The model described in this section is used to compute the target strength as a function of azimuth and frequency for the same cylinder orientation angles and source aspect angles as those used to produce the experimental results of Fig. 4(a). The vertical array tilt angle is the same as in the experiment, and the array responses are broadside beamformed. The results are shown in Fig. 4(d) for the model with second order accurate layered medium Green's functions, and in Fig. 4(e) for the same model with the first order accurate Green's functions. Comparison of the results shows that the consideration of the experimental source-target-receiver geometry contributes to improving the model-data agreement, particularly in the region between 15 and 30 kHz, with azimuthal angles from 10° to 80°. Using the first order approximation of the layered medium Green's function improves the model-data agreement at low frequencies.

A more detailed look at model/data comparisons for a few angles is shown in Fig. 8. Much of the structure seen in the data is also reproduced in both the model of Sec. IV C and the present section. The comparisons indicate that the models capture much of the important physics. However, given that the discrepancies in the nulls around 10 kHz and 20 kHz for broadside and near-broadside angles [Figs. 7(b)–7(d)] are relatively insensitive to variations in the source-target-receiver geometry, there is a need to address the acoustic interaction with the sediment with more accurate models. In particular a three-dimensional FE model that takes into account the contact surface between the target and the sea floor, and a more accurate model of the sea floor reflection coefficient as a function of angle and frequency are two avenues for further effort. The first of these avenues is addressed in the next section.

### E. Fully 3-D code

This section expands on the brief overview in Sec. IV A. The Naval Surface Warfare Center, Panama City Division (NSWC PCD), has developed a high-fidelity, high-speed, frequency-adaptive, 3-D FE acoustic scattering computer simulation system capable of performing $O(10^5)$ 3-D models of complex targets, each with $10^4$ to $10^6$ degrees of freedom

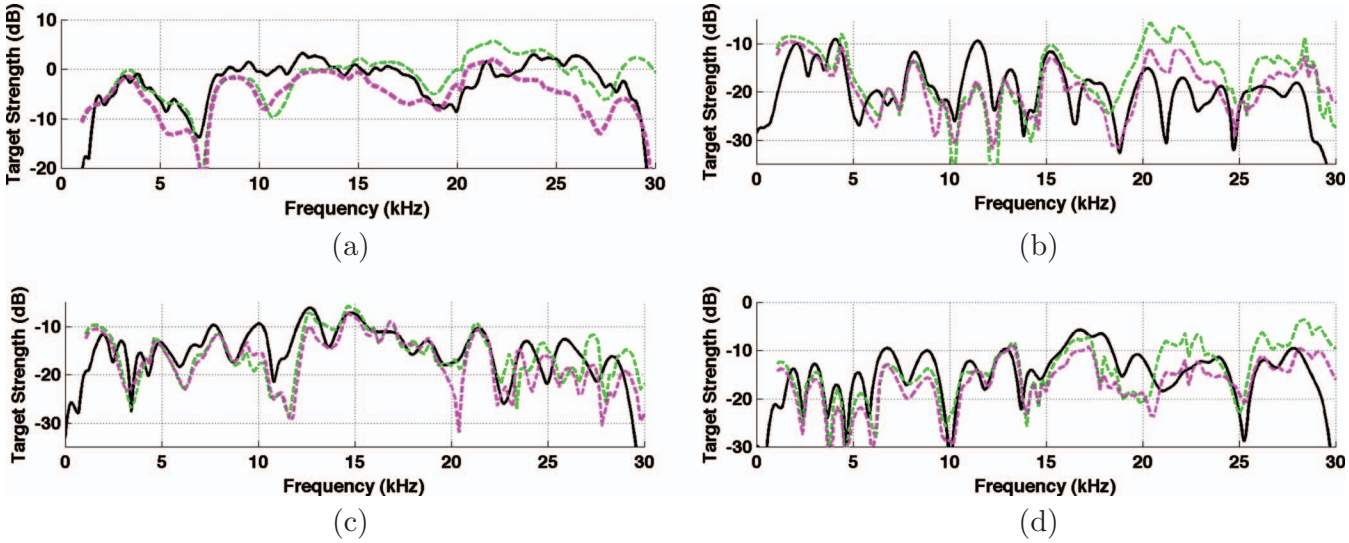


FIG. 8. Comparisons of data (black), FE results using plane wave incident and scattering angles (green), and FE results using experimental geometry with first order accurate Green's function (magenta): (a) broadside [note that the green curve is the same as that in Fig. 6 and magenta curve is the same as the green curve in Fig. 7(e)], (b) 17° relative to broadside, (c) 23° relative to broadside, (d) 33° relative to broadside.

per model, in approximately one day.[7] Scattering in the local region that includes and surrounds the target is modeled using the commercial FE software COMSOL MULTIPHYSICS.[23] This is enhanced by several novel FE modeling techniques developed at NSWC PCD for significantly increasing computational efficiency.[7] Evaluation of the scattered field exterior to the FE model is accomplished using non-FE analytical techniques, viz., the Helmholtz integral, also developed at NSWC PCD.

The FE model has three subdomains (Fig. 9): (i) a hemisphere of water, (ii) a hemisphere of sediment, modeled as a fluid, and (iii) a solid aluminum cylinder, with its axis parallel to the interface and lying almost entirely in the water but slightly buried (0.005 m deep) in the sediment. The hemispherical outer boundaries are located 1.5 wavelengths from the cylinder at all frequencies.

### 1. Uniform modeling error across entire frequency band

Acoustic response as a function of angle and frequency is not an end in itself; it is usually input to detection and classification signal-processing algorithms. The accuracy of those algorithms is significantly increased if the modeling error in the FE calculation is uniform across the entire frequency band. The NSWC PCD software system achieves this by scaling the target-region FE models in two ways: (i) The outer fluid boundaries are located a constant number of incident wavelengths (1.5 in this analysis) from the cylinder at all frequencies, and (ii) the number of finite elements per incident wavelength (3 quadratic elements in this analysis), in all directions, is maintained constant at all frequencies. The NSWC PCD software system automatically controls this scaling.

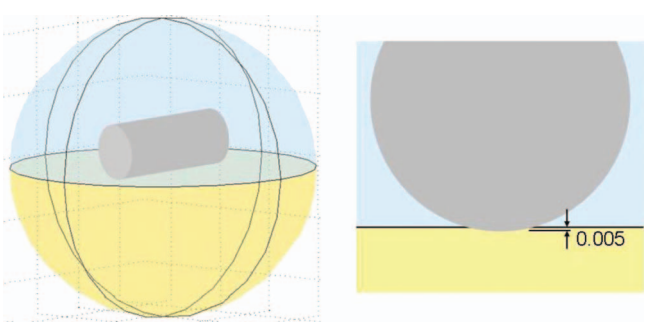


FIG. 9. Left: geometry of FE model for target region. Right: enlarged end view of cylinder.

### 2. Results

*Target strength*: Figure 4(f) is the complete broadband multi-aspect acoustic plot. Target strength was computed every 0.1 kHz from 1 to 30 kHz and every 0.5° from 0° to 90°, a total of 52 671 3-D models. Using an exact (no approximations introduced) symmetry-based domain decomposition technique, each of the 52 671 3-D models was reduced to one quadrant of the geometry in the left panel of Fig. 9. Each quadrant was analyzed four times, each time with a different excitation and different boundary conditions, and the four results were then added. Thus, there was a total of 210 684 3-D FE quadrant analyses. Using quadratic elements throughout the domain, the computational size of the quadrant analyses ranged from 10 K degrees of freedom (dof) at 1 kHz to 813 K dof at 30 kHz. The complete acoustic plot took about 30 h on a 25-blade distributed processing system with two dual-core 3 GHz processors per blade.

Figure 4(f) should be compared with the experimental data in Fig. 4(a). A more precise comparison is shown in Fig. 10(a), which plots the horizontal slices at 0° azimuthal angle (broadside) from both Fig. 4(f) and Fig. 4(a).

Figure 10(a) indicates that most of the experimental/numerical differences are in the range of about 2 to 5 dB. This is quite reasonable, perhaps even better than to be expected, when one considers both the experimental and numerical errors.

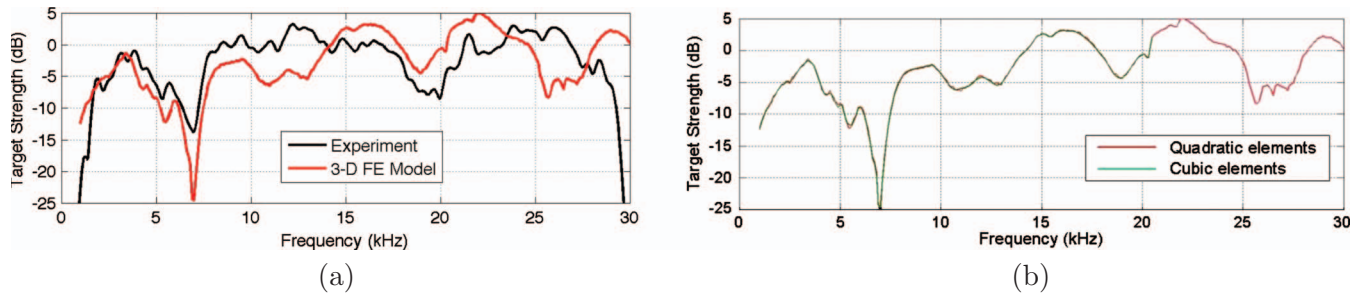


FIG. 10. (a) Comparison of 3-D FE model and experimental data at broadside insonification. (b) Comparison of the FE model results at broadside insonification using quadratic (red) and cubic (green) elements.

On the experimental side, measurements of this type typically have several sources of error, which, collectively, usually amount to about 2 to 3 dB.

On the numerical side, four intentional approximations were made. (1) The incident field in the model is a plane wave, i.e., the source at infinity, which yields a single grazing angle. In the experiment the source is a transmitter about 10 m from the cylinder, which insonifies the cylinder with almost-plane waves with a range of grazing angles. (2) Target strength in the model is computed at a single point, the center of the receive array, whereas the experiment results are derived from summing the array's six elements (recorded separately). (3) The model treats the sediment as an ideal acoustic fluid (with dissipation), ignoring the granularity of the sand-water mixture. (4) The 0.005 m burial depth was only an approximation to a verbal description by one of the divers. Also, the model assumed exactly half a centimeter over the entire length, ignoring actual irregularities in the surface of the sand. This might be a significant source of error, considering that 3-D models of other slightly buried targets have shown noticeable sensitivities to small variations in the burial depths.

*Discretization error*: Another source of numerical error is discretization error, which is inherent in any FE model. However, that error is negligible in this model. Figure 10(b) shows the results of a convergence study. The red curve is the same as the red curve in Fig. 10(a). The green curve is the result of enriching all the quadratic elements to cubic elements; it stops at 20.5 kHz because at that frequency the model contains over one million degrees of freedom, which is close to the limit for an in-core solution. A numerical comparison of the two curves reveals that (i) the mean discretization error is about 0.15 dB, and (ii) the discretization error is quite uniform over the tested band of 1 to 20.5 kHz, as predicted in Sec. IV E 1.

## V. SUMMARY AND DISCUSSION

An experiment examining scattering from an aluminum cylinder placed proud on a water/sand interface has been described and results shown. Those results were compared to FE calculations that included different assumptions. The model/data comparisons show first and foremost that the inclusion of the environment (in this case the water/sediment interface) is essential for accurately predicting the cylinder's target strength as a function of frequency and angle.

The FE modeling was carried out in three ways. The first 2-D/3-D model involved use of multiple 2-D FE calculations for scattering from the cylinder in the free field assuming plane wave incidence and a single scattering angle (receiver at infinity). This was combined with the use of a 3-D image cylinder to treat the scattering from the sand/water interface. The second 2-D/3-D model also used 2-D FE calculations but (i) used the geometry of the experiment, (ii) summed the returns calculated at each receiver element and (iii) used a more accurate two-fluid Greens function. This model demonstrated the sensitivity of data/model comparisons to the experimental geometry.

Neither of the 2-D/3-D models accounted for multiple scattering that can occur between the cylinder and the sand/water interface nor the slight burial of the target. The 3-D model addressed these deficiencies via use of a fully 3-D FE method with (i) the source at infinity (plane wave incidence), (ii) the (point) receiver at a finite distance and (iii) the target slightly buried. Burial depth appears to be important since the 3-D model showed considerable sensitivity to small changes in burial depth. This 3-D model also holds the promise of treating much more complicated targets and waveguide propagation. A future step will be to include the finite range of the source in the 3-D modeling.

From at least an overall qualitative standpoint the 3-D model seems to more accurately capture the target strength behavior for the region identified in previous sections as including contributions from helical waves [frequencies of 15 to 30 kHz with azimuthal angles from 10° to 20°, cf. Fig. 4(a) to Fig. 4(f)]. As noted earlier, this particular region has the potential to be more significantly impacted by the fact that the cylinder is in contact with the sediment. More quantitatively, Fig. 11 shows the same angles as Fig. 8 but with model results separated so that model/data comparisons for each model can be more clearly seen. Generally speaking, each model has particular frequency/angle regions where it is closest to the data.

Of particular interest is the region from 15 to 20 kHz in the last two rows of Fig. 11. This region of angle/frequency has contributions from helical and meridional Rayleigh waves that result in significant enhancements of target strength. For the free field case [cf. Fig. 4(b)] this enhancement is not as large as for the proud case [Fig. 4(a) and Figs. 4(c)–4(f)] indicating the additional contribution from helical and meridional waves excited by the energy that reflects from the sand/water interface.

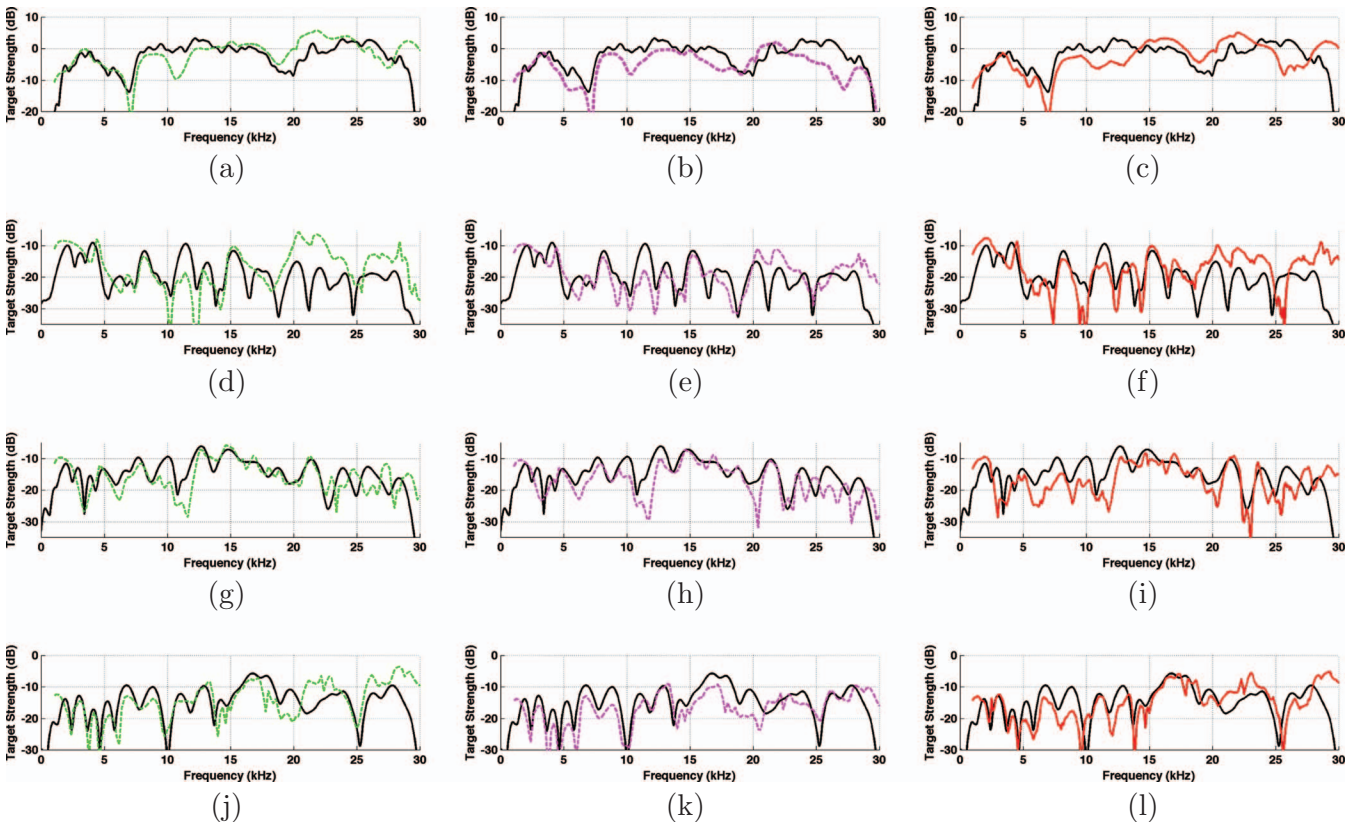


FIG. 11. Comparisons of data (black), FE results using plane wave incident and scattering angles (left column, green curves), and FE results using experimental geometry with first-order-accurate Green's function (center column, magenta curves), 3-D FE results (right column, red curves): top row: broadside, top center row: 17° relative to broadside, bottom center row: 23° relative to broadside, bottom row: 33° relative to broadside.

Differences between models and between data and models are as much as a few dB. However, the overall target strengths as well as the structure seen both as a function of frequency and angle is sufficient to demonstrate the ability of FE modeling to capture the response of the target. There are several effects that the full 3D model can take into account that the axisymmetric model cannot: contact of the cylinder on the sediment, Rayleigh waves (or other circumferential waves) encountering the sediment, and multiple scattering with the sediment. These effects cannot be taken into account with the axisymmetric model as presently formulated. In the future a model-to-model comparison of the second 2D/3D and 3D models, where the experimental geometry is more fully treated (including horizontal offsets of sensors), will be carried out to examine the importance of these model differences.

The level of detail captured by the FE modeling is indicative of the high fidelity possible via these types of calculations. However, understanding the basic physical phenomena that are responsible for the observed features required the insight derivable from complementary physical acoustics modeling. For instance, the dip seen in broadside target strength (for the data and all models) around 7 kHz can be shown to be a direct result of, and very sensitive to, the phase of the water/sediment reflection coefficient. Also, the fact that the major contributors to the target strength measured near $\phi=90°$ are the bistatic paths including a single reflection from the water/sediment interface, is something easily argued via physical acoustics and proven true using the image cylinder model by examining the separate contributions. Similarly, the shorter cylinder required to see a helical wave contribution (Sec. III) is due to a bistatic contribution that includes a single reflection from the interface. In the end, insights derived using the combination/comparison of experiment, physical acoustics and FE modeling may be essential in understanding and predicting the changes caused by the environment and an object's orientation within that environment.

## ACKNOWLEDGMENTS

This work was supported by the Office of Naval Research and the Strategic Environmental Research and Development Program (SERDP) program. The experimental effort owes its success to the extensive engineering and diving support supplied by the APL-UW Ocean Engineering department as well as the complementary technical/logistics support of NSWC PCD.

D.S.B. wishes to acknowledge the following contributors to the 3-D FE modeling effort in Sec. IV: Mr. Les Wigdor for his integration of FE and non-FE modeling systems into a user-friendly GUI-driven 3-D FE system, Dr. Gary Sammelmann for his non-FE analytical techniques for scattering in the exterior region, and Mr. Darshan Bryner for his mathematical support and execution of the many FE models in a distributed-processing environment.

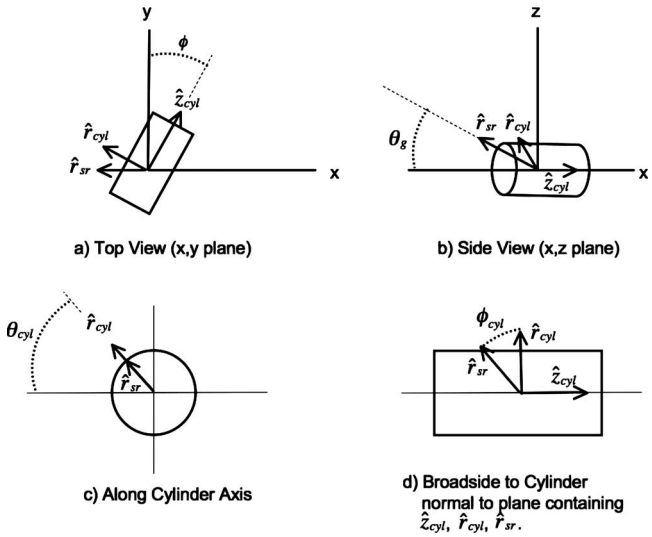


FIG. 12. Definition of angles and unit vectors needed to get $\theta_{cyl}$ and $\phi_{cyl}$ in terms of $\theta_g$ and $\phi$.

The authors also thank Jon La Follett of Washington State University, who made several helpful remarks concerning the material in Sec. III.

## APPENDIX: GEOMETRY AND ANGLE DEFINITIONS FOR SEC. IV C

The goal is to translate the rotations of the cylinder around an axis normal to the plane of the water/sediment interface into the coordinate system defined for the FE calculations.[4,6] That this translation is required can be seen by considering a cylinder rotation in the plane of the water/sediment interface [the defining angle of the experimental results in Fig. 4(a)] from broadside (0°) to end on (90°). Since the source and receiver are above this plane there is never an end-on geometry realized in the experiment. This translation is also needed in order to calculate the bistatic scattering contribution from the image cylinder associated with the single reflection off the water/sediment interface.

Figure 12 defines the geometry needed to obtain the angles required for the FE calculation ($\theta_{cyl}$ and $\phi_{cyl}$) in terms of those of the experiment ($\theta_g$ and $\phi$). Implicit in these definitions is that the source and receiver are at $-\infty$ with an associated grazing angle onto the cylinder and the sediment of $\theta_g$. Also, though the experiment uses a combination of cylinder orientations and movement of the source and receiver along a rail, here the situation is examined as though the source and receiver are stationary and the cylinder rotates through a continuous set of angles $\phi$.

From Fig. 12 the following equations can be determined:

$$\hat{z}_{cyl} = \sin\phi\hat{x} + \cos\phi\hat{y}, \tag{A1}$$

$$\hat{r}_{sr} = \sin\theta_g\hat{z} - \cos\theta_g\hat{x}, \tag{A2}$$

$$\hat{r}_{sr} = \cos\phi_{cyl}\hat{r}_{cyl} - \sin\phi_{cyl}\hat{z}_{cyl}, \tag{A3}$$

where $\hat{z}_{cyl}$ is the unit vector along the cylinder axis and $\hat{r}_{sr}$ is the unit vector pointing toward the source and receiver.

From Eqs. (A1)–(A3) one has

$$\hat{z}_{cyl}\cdot\hat{r}_{sr} = -\sin\phi_{cyl} \tag{A4}$$

and

$$\hat{z}_{cyl}\cdot\hat{r}_{sr} = -\cos\theta_g\sin\phi. \tag{A5}$$

From Eqs. (A4) and (A5) one gets the first of the relations sought, i.e.,

$$\phi_{cyl} = \arcsin(\cos\theta_g\sin\phi). \tag{A6}$$

Equations (A1)–(A3) and (A6) can also be used to get an expression for $\hat{r}_{cyl}$ in terms of $\theta_g$, $\phi$, $\hat{x}$, $\hat{y}$, and $\hat{z}$:

$$\hat{r}_{cyl} = \frac{1}{\sqrt{1-\cos^2\theta_g\sin^2\phi}} \times (-\cos\theta_g\cos^2\phi\hat{x} + \cos\theta_g\sin\phi\cos\phi\hat{y} + \sin\theta_g\hat{z}). \tag{A7}$$

The relation for $\theta_{cyl}$ comes from the dot product of Eq. (A7) with the unit vector perpendicular to $\hat{z}_{cyl}$ in the $x$-$y$ plane, $-\cos\phi\hat{x}+\sin\phi\hat{y}$, giving

$$\theta_{cyl} = \arccos\left(\frac{\cos\phi\cos\theta_g}{\sqrt{1-\cos^2\theta_g\sin^2\phi}}\right). \tag{A8}$$

[1]R. Lim, K. L. Williams, and E. I. Thorsos, "Acoustic scattering by a three-dimensional elastic object near a rough surface," J. Acoust. Soc. Am. **107**, 1246–1262 (2000).
[2]A. Tesei, A. Maguer, W. L. J. Fox, R. Lim, and H. Schmidt, "Measurements and modeling of acoustic scattering from partially and completely buried spherical shells," J. Acoust. Soc. Am. **112**, 1817–1830 (2002).
[3]J. A. Fawcett and R. Lim, "Evaluation of the integrals of target/seabed scattering using the method of images," J. Acoust. Soc. Am. **114**, 1406–1415 (2003).
[4]M. Zampolli, A. Tesei, G. Canepa, and O. A. Godin, "Computing the far field scattered or radiated by objects inside layered fluid media using approximate Green's functions," J. Acoust. Soc. Am. **123**, 4051–4058 (2008).
[5]J. L. Lopes, C. L. Nesbitt, R. Lim, K. L. Williams, E. I. Thorsos, and D. Tang, *Proceedings of the Oceans 2003 MTS/IEEE* (IEEE, San Diego, CA, 2003), pp. 485–493.
[6]M. Zampolli, A. Tesei, F. B. Jensen, N. Malm, and J. B. Blottman, "A computationally efficient finite element model with perfectly matched layers applied to scattering from axially symmetric objects," J. Acoust. Soc. Am. **122**, 1472–1485 (2007).
[7]D. S. Burnett and L. Wigdor, "Acoustic color of elastic objects near boundaries: High-fidelity, high-speed, 3-D finite-element modeling," J. Acoust. Soc. Am. **125**, 2701(A) (2009).
[8]S. K. Numrich, V. V. Varadan, and V. K. Varadan, "Scattering of acoustic waves by a finite elastic cylinder immersed in water," J. Acoust. Soc. Am. **70**, 1407–1411 (1981).
[9]X.-L. Bao, "Echoes and helical surface waves on a finite cylinder excited by sound pulses in water," J. Acoust. Soc. Am. **94**, 1461–1466 (1993).
[10]K. Gipson and P. L. Marston, "Backscattering enhancements due to reflection of meridional leaky Rayleigh waves at the blunt truncation of a tilted solid cylinder in water: Observations and theory," J. Acoust. Soc. Am. **106**, 1673–1680 (1999).
[11]K. Gipson and P. L. Marston, "Backscattering enhancements from Rayleigh waves on the flat face of a tilted solid cylinder in water," J. Acoust. Soc. Am. **107**, 112–117 (2000).
[12]B. T. Hefner and K. L. Williams, "Sound speed and attenuation measurements in unconsolidated glass-bead sediments saturated with viscous pore fluids," J. Acoust. Soc. Am. **120**, 2538–2549 (2006).
[13]D. R. Jackson and M. D. Richardson, *High-Frequency Seafloor Acoustics* (Springer, New York, 2006), pp. 250–251.
[14]P. T. Gough and D. W. Hawkins, "Unified framework for modern synthetic aperture imaging algorithms," Int. J. Imaging Syst. Technol. **8**, 343–358 (1997).
[15]K. Baik, Ph.D. thesis, Washington State University, Pullman, WA, 2008.
[16]K. Baik and P. L. Marston, "Kirchhoff approximation for a cylinder break-

ing through a plane surface and the measured scattering," IEEE J. Ocean. Eng. **33**, 386–396 (2008).
[17]P. L. Marston, "Approximate meridional leaky ray amplitudes for tilted cylinders: End-backscattering enhancements and comparisons with exact theory for infinite solid cylinders," J. Acoust. Soc. Am. **102**, 358–369 (1997).
[18]P. L. Marston, in *Acoustical Imaging*, edited by S. Lees and L. A. Ferrari (Plenum, New York, 1997), pp. 369–374.
[19]F. J. Blonigen and P. L. Marston, "Leaky helical flexural wave backscattering contributions from tilted cylindrical shells in water: Observations and modeling," J. Acoust. Soc. Am. **112**, 528–536 (2002).
[20]A. Bayliss, M. Gunzberger, and E. Turkel, "Boundary conditions for the numerical solution of elliptic equations in exterior regions," SIAM J. Appl. Math. **42**, 430–451 (1982).
[21]A. D. Pierce, *Acoustics* (Acoustical Society of America, Woodbury, NY, 1989), Chap. 4.
[22]F. Ihlenburg, *Finite Element Analysis of Acoustic Scattering* (Springer, New York, 1998).
[23]COMSOL MULTIPHYSICS User's Guide, Version 3.4 (2007).

# Acoustic Response of Unexploded Ordnance (UXO) and Cylindrical Targets

Steven G. Kargl and Kevin L. Williams
Applied Physics Laboratory
University of Washington
1013 NE 40th St
Seattle WA 98105
Email: kargl@apl.washington.edu

Timothy M. Marston
Physics and Astronomy Dept.
Washington State University
Pullman, WA 99164-2814

Jermaine L. Kennedy
and Joseph L. Lopes
Naval Surface Warfare Center
Panama City Division
Panama City, FL 32407-7001

***Abstract*— A series of monostatic and bistatic acoustic scattering measurements were conducted to investigate discrimination and classification capabilities based on the acoustic response of targets for underwater unexploded ordnance (UXO) applications. The measurements were performed during March 2010 and are referred to as the Pond Experiment 2010 (PondEx10), where the fresh water pond contained a sand sediment. The measurements utilized a rail system with a mobile tower and a stationary sonar tower. Each tower is instrumented with receivers while the sources are located on the mobile tower. For PondEx10, eleven targets were deployed at two distinct ground ranges from the mobile tower system. Acoustic data were initially processed using synthetic aperture sonar (SAS) techniques, and the data were further processed to generate acoustic templates for the target strength as a function of frequency and aspect angle. Preliminary results of the processing of data collected from proud targets are presented. Also presented are the results associated with a processing technique that permits isolation of the response of an individual target, which is in close proximity to other targets.**

## I. Introduction

Although the practice of disposing conventional and chemical munitions in coastal waters was discontinued during the 1970's, the environmental, economical, and even the recreational impact persists today [1]. In Overfield and Symons' overview of the Resources and UnderSea Threats (RUST) database [2], they note that 2100 underwater sites are likely to contain munitions. Of those 2100 sites, verification has been completed on only slightly more than 50%. Schwartz and Brandenburg [3] summarize the current technologies available for underwater UXO applications. Their Table 1 includes metal detection (e.g., electromagnetic induction and magnetometers), chemical sensors (spectroscopy and fluorescence), and sonar. Metal detection and chemical sensors are typically restricted to short ranges; while the sonar technologies considered are limited in range (e.g., Didson system) or are limited by poor penetration into sediments (e.g., side-scan sonar) due to the high frequencies used. Furthermore, Schwartz and Brandenburg note that SAS is still a relatively new technology in UXO detection and that low-frequency SAS systems have demonstrated detection of proud and partially buried objects [4].

Low-frequency SAS systems with a wide bandwidth have several advantages over higher frequency sonar systems. Low frequencies offer greater detection ranges, which permits the surveying of wider areas. In addition, low frequencies attain greater penetration depths into sediments, which permit detection of partially and completely buried munitions. The range resolution of a SAS system is related to the bandwidth of the transmitted signal where a wider bandwidth provides higher resolution. Thus, we report here on our preliminary analysis of UXO detection and discrimination by a low-frequency wide bandwidth SAS system. Our work compliments that of Bucaro *et al.* [4] in that they consider isolated UXO in their research. The experiments conducted during PondEx10 have multiple UXO in the field of view of the SAS system with a minimum separation distance of 1.5 m.

## II. Pond Experiment 2010

PondEx10 was carried out in a fresh water pond located at the Naval Surface Warfare Center, Panama City Division (NSWC PCD). This pond holds approximately 9 million gallons of water, and has nominal dimensions of 110 m in length and 80 m in width. The water depth at the location of the deployed target fields is $\sim 14$ m. A $\sim 1.5$ m thick layer of medium-fine sand covers the bottom of pond. To prevent biological growth and fouling of the targets and equipment, the water is filtered and chlorinated. During the PondEx10 exertions, the sound speed in the water, which was determined from temperature measurements acquired from the divers, was found to be 1456 m/s. A detailed drawing and aerial view of the pond can be found in [5].

Eleven targets were deployed in the measurements. The targets included a solid aluminum cylinder, an aluminum pipe, an inert 81 mm mortar (filled with cement), a solid steel artillery shell, two machined aluminum UXO, a machined steel UXO, a de-militarized 152 mm TP-T round, a de-militarized 155 mm empty projectile (without fuse or lifting eye), a small aluminum cylinder with a notch, and two rocks with sizes comparable to the UXO targets. Figure 1 shows a few of the UXO and generic shapes used. The machined UXO, based on a CAD drawing of the solid steel artillery shell, were constructed from materials with known properties. The aluminum cylinder is 2 ft long with a 1 ft diameter; while the pipe is 2 ft long with an inner diameter of 1 ft and 3/8 inch wall thickness.

Fig. 1. A selection of targets used during PondEX10. From left to right, the targets are a machined aluminum UXO, solid steel artillery shell, small aluminum cylinder with a notch, de-militarized 152 mm TP-T round, 81 mm mortar, and de-militarized 155 mm UXO. Rock 2 is in the foreground.

A rough layout of the 10 m target field is illustrated in Fig. 2. Divers first deployed a 21 m long rail system, which consists of three independent sections (see Fig. 1 in [5]). The sections are connected and leveled to establish a baseline for the geometry of the experiment. The divers then surveyed in two screw anchors at an 11 m ground range from the rail, where the dashed lines in Fig. 2 depict temporary lines for placing the left screw anchor. A lightweight guide line is then stretched between the screw anchors and marked at 4, 7, 10, 13, and 16 m from the left screw anchor. These locations are enumerated as Target Patch #1 through #5, and mark the sites of 1 $m^2$ patches, where targets are deployed (dark blue patches in Fig. 2). When seven targets are present, the additional two targets are placed in 1 $m^2$ patches between Target Patches #2 and #3 and Target Patches #3 and #4 (light blue patches in Fig. 2).

Target Patches were created by the divers using a set of T-bar aluminum rails that are registered against the 11 m guide line. One T-bar aluminum rail, referenced to the guide line, is driven into the sediment while the second rail is placed meticulously parallel with the first T-bar with a separation distance of $\sim$ 1 m. The second T-bar is then driven into the sediment, and the rails are checked for levelness. Divers smooth the sand interface by scraping a third aluminum bar, which is perpendicular to the two T-bar rails, along these rails. Low spots, if observed, are filled with sand from outside the target field. This procedure is followed prior to a set of measurements, where the targets are rotated though a set of orientations (relative to rail).

To orient the targets, a square PVC frame with dimensions comparable to the target patch is utilized. One side of the frame is referenced to the 11 m guide line, which enables all four sides of the frame to encompass a Target Patch. A series of holes in the frame allowed the divers to select one of several angles. The angles used in PondEx10 for targets with cylindrical symmetry ranged from -80° to 80° in 20° increments. A target is broadside to the rail system at 0° with the nose of a UXO pointing towards a stationary tower. The nose (tail) of a UXO pointed towards the rail in the -80° (80°) orientation. For the rocks, the rotations covered -80° to 260° due to their asymmetry.

The mobile tower is placed on the rail system, and it holds acoustic sources and receivers. The mobile tower moves at 0.05 m/s with the source transmitting a ping every 0.5 s. The total distance traveled along the rail is 19 m. Thus, a SAS data set contains 760 pings, and each data set is referred to by a "sequence number". The receiver on the mobile tower is a six channel vertical array, where each channel is recorded separately at a 1 MHz sample rate. The acoustic receivers located on the stationary sonar tower (see Fig. 2) were mounted on horizontal pan and vertical tilt motors, which allowed accurate alignment of the main lobe of the receivers with the Target Patches. The stationary receivers recorded data at a 500 kHz sample rate. The sources and receivers on both the rail system and stationary sonar tower stood about 4 m above the water-sand interface. When traveling from left-to-right in Fig. 2, the source transmitted a 6 ms LFM chirp centered at 16 kHz with 30 kHz of bandwidth. On the return trip, the source transmitted a 4 ms LFM chirp centered at 40 kHz with 20 kHz of bandwidth.

Two target fields were deployed during the course of PondEx10: one with targets at 10 m ground range from the rail system and one with targets at 5 m ground range. At a 10-m ground range, the targets were proud on a flattened water-sand sediment interface; while the targets were either proud, half-buried, or flush buried when placed at 5 m. The 10 and 5 m ranges correspond to $\sim 20°$ and $\sim 40°$ grazing angles with respect to the source and receiver locations, respectively. The critical grazing angle for the sand sediment in the test pond was nominally $28°$. Thus, data collected for the proud targets were at shallow and steep grazing angles; while data collected for the half-buried and fully buried targets corresponded to a steep grazing angle case. When five targets were placed in the target field, the separation distance between adjacent targets was approximately 3 m. This distance was selected to minimize multiple scattering between targets. When the additional two targets were inserted into the target field, the separation distance was reduce to 1.5 m for the inner five targets.

## III. Data Processing and Discussion

The data were initially processed using time-domain and frequency-domain synthetic aperture sonar (SAS) techniques in which high resolution images were generated. A brief description of the time-domain method follows. First, a raw SAS data set is pulse compressed by match filtering the pings with a replica of the transmitted LFM chirp. During the match filtering, a Hilbert transform converts the real-valued recorded pings to complex-valued signals. Next, baseband pulse-compressed data is obtained by removing the carrier

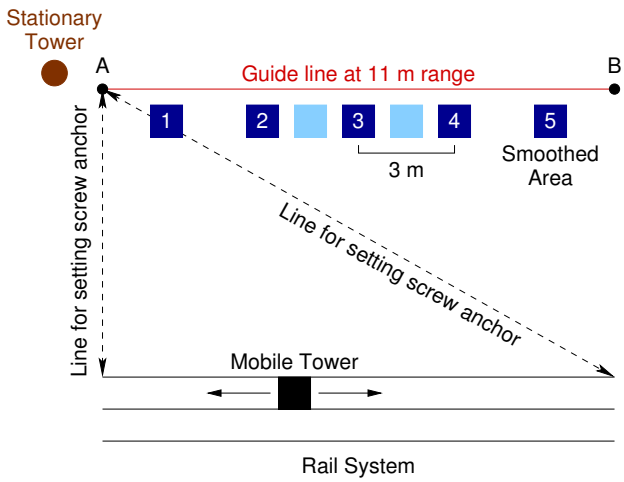


Fig. 2. Schematic layout of the target field. The left and right screw anchors are denoted by 'A' and 'B'.

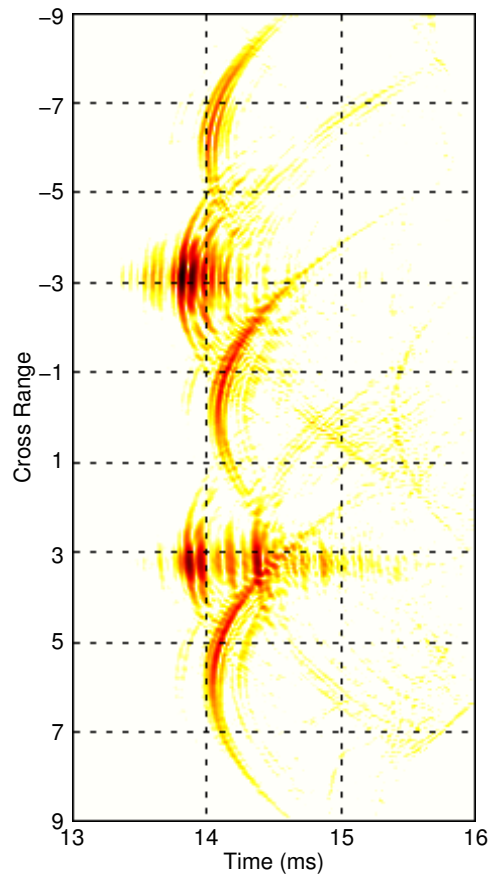


Fig. 3. Baseband pulse-compressed data for sequence 27. The image is normalized by the maximum value in the data and displayed on a 0 to −30 dB color scale.

frequency, i.e., multiplying by $\exp(\imath\omega_0 t)$, where $\omega_0$ is an angular carrier frequency and our processing scheme assumes a negative time convention. Figure 3 shows the magnitude of the baseband pulse-compressed pings for sequence 27, which used the 1–31 kHz LFM chirp. This sequence included (from top to bottom in Fig. 3) the machined aluminum UXO #1, 2:1 solid aluminum cylinder, machined steel UXO, 2:1 aluminum pipe, and the solid artillery shell in a proud, broadside orientation. It is immediately evident that the scattered acoustic field from the individual targets interfere with their neighbors. The overlap of the scattered acoustic fields has an important consequence for the acoustic template processing discussed below. However, for SAS processing the coherent addition of the complex time signals is unaffected by this overlap. The next step to produce a SAS image from the time-domain data is to use a simple delay-and-sum beamformer [6]. For each pixel in a SAS image, the signals are time shifted to account for propagation from the source to the pixel and then from the pixel to the receiver. Once the time shift is performed, the signals are coherently added to determine a complex reflectivity of the pixel. This time shifting is done for each pixel in a SAS image. Images for individual channels of the receive array as well as the superposition of the six channels have been constructed.

SAS images for the targets in sequence 27 are shown in Fig. 4. These images are $1 \times 2$ m$^2$ patches with a 1 cm$^2$ resolution, where the six channels of the receive array have been summed. The relative dB scale is determined from the magnitude of the "hottest" pixel with the two-way spreading loss removed.

Figure 3(a) in [5] is a SAS image of the same solid aluminum cylinder obtained in the previous year's PondEx09 measurement, and it is similar to Fig. 4(b) shown here. Williams *et al*. developed an acoustic ray model (see Fig. 5 in [5]) to understand the observed triplet structure. Briefly, the rays that contribute to this structure are: (1) a specular ray directly reflected from the cylinder; (2) a ray reflected from the cylinder that then reflects from the water-sand interface; (3) a ray reflected from the water-sand interface that reflects from the cylinder; and (4) a ray reflected from the water-sand interface reflects from the cylinder and then follows its incoming path to reflect once again from the sediment. The features beyond the triplet structure has been associated with the elastic response of the target.

The geometric shape of the targets in Figs. 4(a), (c), and (e) are identical. In Fig. 4(a), the triplet structure observed with the solid cylinder is again seen. Given the cylindrical symmetry of these targets, it is not unexpected to observe a similar structure. The triplet structure is not observed in (c) and (e). This may be a consequence of the "brightness" of the steel targets, the small time difference in the arrival of the four ray paths to the receiver, and the 20 dB range used to display the image. Comparison of these images also shows that the aluminum target has a much weaker feature following the main geometric response. This suggests over the frequency range of the LFM chirp, the machined aluminum UXO has a much different elastic response in comparison to the machined steel UXO and the solid steel artillery shell. Finally, in (c) the feature near 10.75 m is due to a screw anchor that was inadvertently left in the target field during the collection of sequence 27.

The final SAS image to consider is that of the aluminum

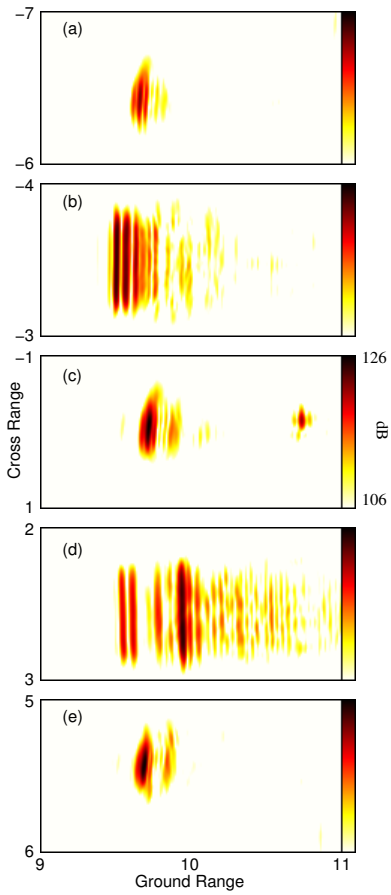


Fig. 4. SAS images of the targets in for sequence 27: (a) machined Al UXO #1, (b) solid Al cylinder, (c) machined steel UXO, (d) Al pipe, and (3) solid artillery shell.

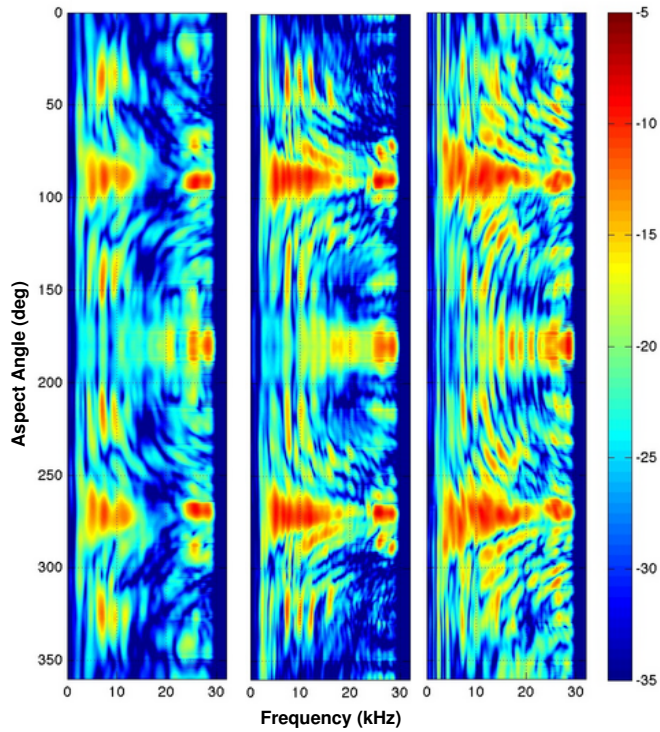


Fig. 5. Acoustic template for for the machined Aluminum UXO #1 (left), machined steel UXO (center), and (3) solid steel artillery shell (right).

pipe in Fig. 4(d). The triplet structure is no longer found and instead a doublet appears. A physical acoustics based ray model has yet to be constructed. Presumably, one or more reflection coefficients needed in the ray models for the water-filled cylindrical shell may lead to a destructive interference of some of the ray paths. The bright return at 10 m is associated with an acoustic field that is transmitted into the pipe and reflected from the far side. The other observed structure probably is due to an elastic response of the pipe. Finite element modeling of this experimental situation is an on-going task.

The data were further processed to generate acoustic templates of the target strength as a function of frequency and aspect angle. Due to the relatively small separation distances between the UXO targets, the scattered fields from the targets overlap (see Fig. 3). To generate an acoustic template, a novel SAS filtering technique was used to isolate the response of an individual target and to suppress reverberation noise. The details of the SAS filtering will be given elsewhere. A brief summary is as follows. The raw SAS data set is deconvolved with a target arc (i.e., point spread function) for a single selected location in an image plane, and a SAS image is formed. As an observation point in the SAS image moves away from the selected location, the image becomes defocused because the target arc is not appropriate for distant locations. The SAS image is then windowed in the spatial domain about the selected location. This windowed image contains the information to reconstruct the time signals associated with a given target via a convolution with the same target arc. It is noteworthy that the deconvolution and convolution processes are linear operations, and hence in the absences of multiple scattering the recovered signal isolates the response of the selected target.

Inspection of the target arcs in Fig. 3 suggests that, at most, an aspect angle range for a given target in a given sequence spans approximately $\pm 15°$. This motivated the choice of target rotations from $-80°$ to $80°$ in $20°$ increments. Thus, adjacent rotation angles provide an overlap in the aspect angle ranges (e.g., $20° \pm 15°$ and $40° \pm 15°$), which permits the nine sequences to be stitched together to form the acoustic templates in Fig. 5. The overlapping regions were determined by a cross-correlation of the aspect angle ranges for adjacent rotation angles. Once the overlap was established, the two ranges are merged by a smoothing operation over the overlap region.

A cursory inspection of Fig. 5 reveals that the structure observed for the machined steel UXO is a better match to the steel artillery than the machined aluminum UXO. In this figure, $90°$ and $270°$ correspond to a broadside orientation, $0°$ and $360°$ have the nose of the ordnance pointing at the rail system, and $180°$ corresponds to the tail pointing toward the

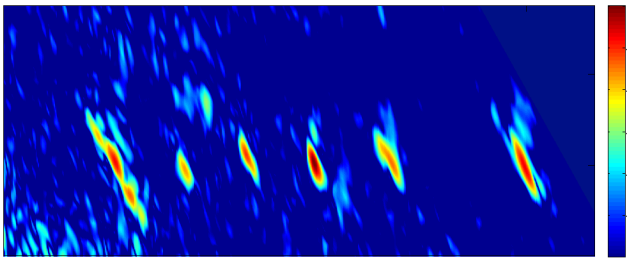

Fig. 6. Bistatic SAS image for sequence 258.

rail. Currently, finite element models of these UXO are being constructed to investigate the observed acoustic templates. Based on the results of Williams *et al.* and Bucaro *et al.*, it is anticipated the observed differences are associated with the elastic response of the target [4], [5].

Figure 6, generated from sequence 258, is an example of the bistatic images generated by processing data using SAS methods. The source on the mobile tower rail system transmitted an acoustic signal, which was a 4 ms LFM chirp with a 40 kHz carrier frequency and 20 kHz bandwidth. While it traveled the length of the rail, the receivers on the stationary tower were utilized to record the scattered signals for six targets in the field 10 m from the mobile tower. This sequence included (from left to right) the 152 mm TP-T round, aluminum cylinder with notch, solid steel artillery shell, inert 81 mm mortar (filled with cement), machined aluminum UXO #1, and the 155 mm empty projectile. These targets were all in a proud configuration oriented at 40° with respect to the mobile tower rail system. The image reveals the target separation for the first five targets (from left to right) were $\sim 1.5$ m corresponding to the minimum separation distance examined during PondEx10; while the last target had a separation distance of 3 m from the fifth target. In this image the color scale corresponds to a logarithmic scaling of the scattered intensity relative to the image maximum over a 30 dB range. Interpretations harvested from a host of bistatic sequences acquired during these experiments are currently being processed with the intentions of implementing additional finite element modeling to explain and decipher the results.

## IV. Conclusion

The preliminary analysis of PondEx10 SAS data sets suggest that low frequency wide bandwidth SAS systems are capable of UXO detection and discrimination. Work remains to demonstrate that the acoustic template for a given UXO can be used as a fingerprint to uniquely identify a detected target as a UXO. The results of a finite element model analysis of the solid cylinder and partial results for the pipe have shown the complex structure found in their acoustic templates can be directly related to an elastic response of the target. Finite element models for the various UXO in our experiments are currently under investigation, where it is anticipated that the structure observed in Fig. 5 may be reproduced. Finally, the current method for the construction of the acoustic templates demonstrates that the SAS filtering technique and the merging of aspect angle ranges via correlation and smoothing techniques provide a robust approach to acoustic template generation.

## Acknowledgment

Partial support was provided by The Strategic Environmental Research and Development Program (SERDP) under projects MM-1665 and MM-1666 and by the Office of Naval Research.

## References

[1] Terrence P. Long, "A global prospective on underwater munitions," *Mar. Technol. Soc. J.*, **43**, 5–10 (2009).

[2] Mike L. Overfield and Lisa C. Symons, "The use of the RUST database to inventory, monitor, and assess risk from Undersea Threats," *Mar. Technol. Soc. J.*, **43**, 33–40 (2009).

[3] Andrew Schwartz and Erika Brandeburg, "An overview of underwater technologies for operations involving underwater munitions," *Mar. Technol. Soc. J.*, **43**, 62–75 (2009).

[4] J. A. Bucaro, B. H. Houston, M. Saniga, L. R. Dragonette, T. Yoder, S. Dey, L. Kraus, and L. Carin "Broadband acoustic scattering measurements of underwater unexploded ordnance (UXO)," *J. Acoust. Soc. Am.*, **123**, 738–746 (2008).

[5] Kevin L. Williams, Steven G. Kargl, Eric I. Thorsos, David S. Burnett, Joseph L. Lopes, Mario Zampolli, and Philip L. Marston, "Acoustic scattering from a solid aluminum cylinder in contact with a sand sediment: Measurements, modeling, and interpretation," *J. Acoust. Soc. Am.*, **127**, 3356–3371 (2010).

[6] Steven G. Kargl, Kevin L. Williams, Eric I. Thorsos, and Joseph L. Lopes, "Bistatic synthetic aperture sonar measurements and preliminary analysis," in *Boundary Influences in High Frequency, Shallow Water Acoustics*, N. G. Pace and P. Blondel (Eds.), University of Bath, UK, Sept., 2005, pp. 137–143.